Czech Technical University in Prague
Faculty of Biomedical Engineering
Department of Natural Sciences

Nitrogen soft X-ray source for imaging of biological objects

Doctoral Thesis

Ing. Šárka Salačová

Kladno, January 2020

Ph.D. Programme: Biomedical and clinical technology

Supervisor: prof. Ing. Miroslava Vrbová, CSc.
Supervisor-Specialist: Ing. Pavel Vrba, CSc.

Abstract:

Soft X-ray radiation sources usable for microscopy have been studied in the laboratory XUV at CTU Faculty of Biomedical Engineering. This thesis is focused on the optimization of generation quasi-monochromatic radiation with a *water window* wavelength of 2.88 nm. The source of radiation is a laser plasma created in Nitrogen gas-puff target.

The optimization function is delineated in chapter 1.5.1. Gradually, the effect of system parameters on the output energy is investigated.

For the microscopic imaging, we need high energy in a single shot at the output of the SXR source. The biggest effect on the output of pulse energy has a mass density ρ spatial distribution in the gas-puff target. We studied it via laboratory experiments and computer modelling. In chapter 4.1, we supply information about the effect of nozzle ageing and investigation of double stream nozzle.

We used Z star code to construct a complete model of the gas-puff target. In chapter 4.2, the results of computer modelling are compared with experimental data. This comparison is very important as the Z star code (developed for plasma magnetohydrodynamics) has not yet been used for gas flow simulations.

Plasma radiation, modelled by the Z-star code, is given in chapter 5. The computer model of the source may be further used for the design of improved SXR source.

We paid attention also to biological samples and after a literature search, we present results of SXR microscopy image of CT 26 fibroblasts, derived from colon carcinoma Mus musculus (strain BALB/c) in chapter 6.

Key words: soft x-ray radiation, laser-produced plasma source, gas-puff target, CT 26 fibroblasts sample

Contents

Introduction

Presently, many methods exist for biological objects imaging. The oldest and well known method is imaging with the optical microscope. An optical microscope typically achieves a magnification of 50× to 1000× [1]. However, this method has its limits. The magnification is given by Abbe criterion $d = \lambda/A$ and depends on used wavelength. Optical microscope can image a tissue or cell but it can not image inner structures of a cell. Many of the researchers are trying to image smaller objects like organelles with good-quality resolution. This leads to exploring new methods that can give us information on μm size structures or smaller ones.

In this thesis we are focused on SXR source that could be used as base for SXR microscope. Soft x-ray radiation (SXR) is defined as photon energies of about 250 eV to several keV [2] which means that we can depict structures smaller then 1 μm. For biological imaging, we can, moreover, use the different absorption of Carbon and Hydrogen in the *water window* region (region between K-absorption edge of Oxygen at the wavelength of 2.34 nm and the K-absorption edge of Carbon at 4.4 nm). Nearly all SXR radiation is absorbed in proteins and water is transparent for SXR radiation. This effect allows to image live structures in the water environment. Well known and used device emitting radiation in this region and used for SXR microcopy is synchrotron [3]. Big advantage of synchrotron is high intensity that allows to use the microscope in single shot mode and use live specimens [4]. Unfortunately, microscope based on synchrotron radiation is not applicable in conventional biological laboratories. This leads to start an aspiration to build compact SXR microscope.

One of the possibilities how substitute the synchrotron radiation is to use laser-produced (LPP) or discharge-produced (DPP) plasma source [5, 6]. Currently some laboratories build compact microscopes [7, 8]. In general, the compact SXR microscopes use as base the LPP table-top SXR sources based on solid [9], liquid [10] or gas [11] target. The sources emit radiation due to used element with broad spectrum or on one wavelength.

A big disadvantage of the SXR source is attenuation. The plasma radiation is absorbed in air [12] and now all measurements have to be done in vacuum chamber. The goal for all table-top SXR system is to have enough photons per steradian so that radiation can be used outside the chamber and the sample is imaged in a natural water environment.

We are working on optimization the SXR source placed in XUV laboratory at FBME CTU as a base for SXR microscope and developed the computed model for entire system that allow us to design new improved of the source.

1 State of the Art

1.1 Microscopes for Imaging of Biological Objects

Since 17^{th} century, when the first microscopes were composed, the imaging of small structures has come a long way. At the beginning of 20^{th} century August Köhler introduced illumination system [13], design used till today. Next significant step was invention of confocal scanning microscopy that allows three-dimensional imaging through optical sectioning [14].

For imaging structures smaller then 1 μm the electron microscope was developed [15]. It uses high-energy electrons with a de Broglie wavelength much shorter than visible light. For biology and material research are used the transmission or scanning electron microscopy and they offer resolution on atoms level. However, the biological samples are limited to a few hundreds nanometres [16]. Here comes the new discovery from W. C. Röntgen, the x-rays [17]. Unfortunately, it took half century before the first microscope using x-rays was developed and the biggest progress was done after development of zone plate optics and synchrotron sources.

The x-ray microscopes operate on wavelengths < 10 nm. If the objective is to develop SXR microscopy [18, 19, 20] of biological samples [21, 22, 23] the preference is given to radiation with a wavelength in the *water window* spectral range (i.e. 2.3 – 4.4 nm) [2]. In this spectral range, a high contrast between the absorption of water and organic molecules containing carbon is achieved.

The Göttingen group has been operating transmission x-ray microscope of ever-improving performance since 1974 [8]. The basic approach has been to use a zone plate as a microscope objective to create a magnified image of the object. This microscope used synchrotron radiation that can not be used in biological laboratories. It started development of compact x-ray microscope.

High-resolution transmission X-ray microscopy was first developed by Schmahl et al. at the university of Göttingen in Germany in 1993 [24]. In 1998 Ch. Spielmann, from Technische Universität in Wien, presented a compact x-ray source based on a thin helium gas jet. The jet was exposed to an on-axis peak intensity of $\approx 5 \times 10^{15}$ W/cm^2 with 5-fs pulses. The source brightness at $\lambda = 4.4$ nm was estimated as $> 5 \times 10^8$ photons/sr $\times$ line $\times$ pulse [25]. First table-top soft x-ray full-field transmission microscope based on a droplet-target laser-plasma source, demonstrating reproducible sub-visible

resolution imaging with good signal-to-noise ratio, was developed by Berglund, Hertz et al. in year 2000 [26]. A solid-carbon-target laser plasma has been combined with an elliptical condenser and a zone plane objective to perform imaging of dry test objects. Laser pulses from 10 Hz, 100 ps frequency-doubled Nd:YAG laser are focused onto 15 mm diameter ethanol droplets, which are generated by a piezo-electrically vibrated glass capillary nozzle. The microscope operates at $\lambda = 3.37$ nm. Ethanol was used as target liquid. The flux was typically $\sim 10^{12}$ photons/(sr $\times$ pulse) and the source diameter (FWHM) was ~ 25 μm. Images of dry test samples are recorded with exposure times of a few minutes and show features smaller than 60 nm.

In Table 1 is shown the overview of some SXR sources with similar wavelength in *water window* region. All sources are from category of table-top SXR source that could be used in biological laboratories. All marked sources were used in SXR microscopy. Source 1 was presented by Wachulak, Bartnik in 2012 [28], and in microscope was used Mo/Si multilayer ellipsoidal mirror (condenser) with 80 mm in diameter. Source 2 was presented in the same year by Legall and Blobel [29] and condenser zone plate of 9 mm diameter was used. Last one was published by Kishimoto and Kado [31]. They used simple ellipsoidal mirror.

Type	λ **[nm]**	**Plasma spot size [mm]**	**Brightness [ph/srad]**	**Resolution [nm]**	**Input Laser**	**Ref.**
Nitrogen gas-puff target	2.88	0.4×0.2	2.88×10^{12}	<50	Nd:YAG, 600 mJ	Kladno, [27]
Argon gas-puff target[1]	2.88	0.24×0.13	1.3×10^{13}	<50	Nd:YAG, 740 mJ	Warsaw, [28]
Liquid-Nitrogen-cryo jet[2]	2.48	r = 0.015	10^{12}	100	Nd:YAG (2ω), 150 mJ	Stockholm, [29]
Liquid-ethanol target	3.37	r = 0.025	10^{12}	-	Nd:YAG, 800 mJ	New York, [26]
Nitrogen gas-puff target	2.88	r = 0.5	1.18×10^{13}	<80	Nd:YAG, 600 mJ	Göttingen, [30]
Au film target[3]	3.10	r = 0.05	10^{14}	150	Nd:Glass, 10 J	Kyoto, [31]

Table 1: *Table-top soft x-ray sources emits in water window spectral range. Sources marked* [1,2,3] *were used in SXR microscopes (technique is described above).*

1.2 Absorption Properties of Selected Materials in *Water Window* Spectral Range

X-rays interaction with matter is based on an interaction with both free and bounded electrons. The possible interaction processes are: elastic or inelastic scattering, and photoelectric absorption [32]. The elastic scattering from free electrons is called Thomson scattering, while for strongly bounded electrons is called Rayleigh scattering. In inelastic or Compton scattering a small fraction $\Delta E = (1 - cos\theta)E^2/m_e c^2$ of the photons energy E is transferred to an electron with mass m_e, making it recoil [33]. This scatters the photon in an angle θ and shifts the photon energy accordingly. Photoelectric absorption occurs when the photon is absorbed and all its energy is transferred to the electron. Soft x-ray photon energies are similar to the binding energies of inner-shell electrons, which results in strong interaction via absorption.

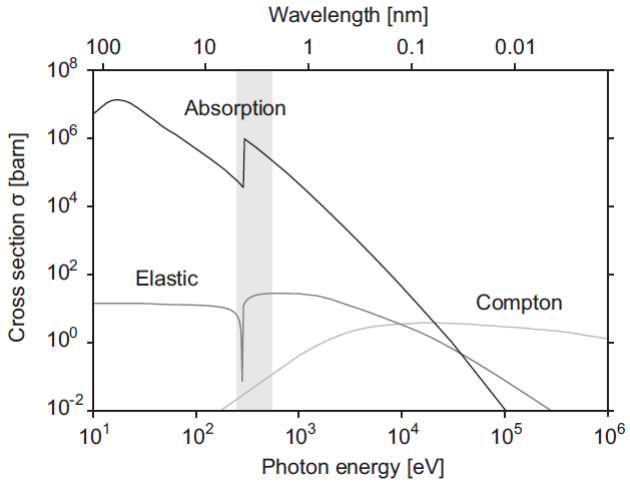

Fig. 1: *Scattering and absorption cross-sections for carbon. Photoelectric absorption is the most dominant process for soft x-rays in the water window (shaded area). All interactions decrease with energy but scattering decreases slower and therefore becomes the dominating process above 20 keV. [34]*

The interaction of soft x-rays with atoms is described by the atomic scattering factor $f = f_1 - if_2$. It is an element-specific strongly varying analytic function of photon energy, especially near electron binding energies. Its real and imaginary parts are related by the Kramers-Kronigs relation [35]. The complex index of refraction n describes the optical properties of material and, in the case of forward scattering, it relates to the atomic scattering factor by:

$$n = 1 - \delta + i\beta = 1 - \frac{n_a r_e \lambda^2}{2\pi} (f_1 - i f_2) \tag{1.1}$$

where n_a is the average density of atoms, $r_e = 2.818 \times 10^{-15}$ m the electron radius and λ the wavelength. For solid or liquid materials in the *water window* δ is typically in the order of 10^{-3}, while β varies between 10^{-5} - 10^{-3}. The real part, $1 - \delta$, determines the phase velocity, which after a propagation distance z results in a phase shift given by:

$$\Delta\varphi(z) = \varphi_0(y) - \varphi(y) = \frac{2\pi\delta}{\lambda} z \tag{1.2}$$

where $\varphi(y)$ and $\varphi_0(y)$ are the acquired phases in the material and in vacuum along the axis y. The imaginary part, β, relates to an exponential decay of the intensity I_0 according to Beer-Lambert's law:

$$I(z) = I_0 e^{-\frac{4\pi\beta}{\lambda} z} = I_0 e^{-\mu z} \tag{1.3}$$

where μ is the absorption coefficient of the material.

As is shown in Figure 2, the *water window* provides natural absorption constant for biological samples.

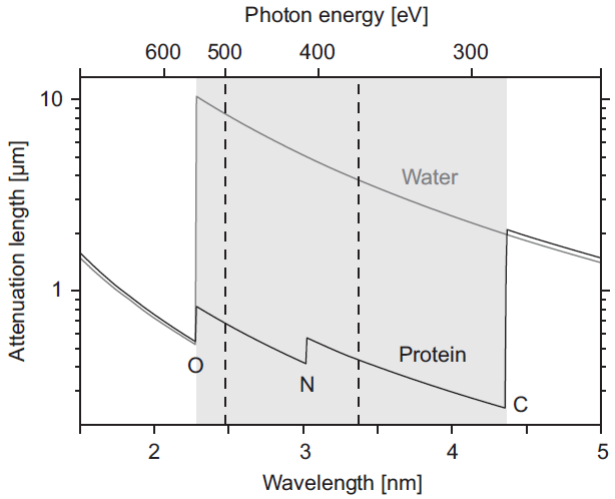

Fig. 2: *Water window absorption contrast. The difference in absorption for protein and water acts as a natural contrast mechanism for biological samples. [2]*

The interaction between matter and soft x-rays also determines the properties of

optical elements that can be used (Fig. 3). The small ratio between the phase shifting δ and absorbing β properties of elements make refractive optics infeasible. The reflectivity is small because $n \approx 1$. However, since the phase velocity in matter exceeds the speed of light in vacuum ($\delta > 0$), total external reflection can be used for efficient reflective optics. And even though refraction is small ($\delta < 10^{-2}$) it is enough to give a substantial phase shift in a few 100 nm of material, which can increase the efficiency of diffractive optics. Also the transmission in Nitrogen (air) for normal pressure is problem, so we need to work in high or ultra-high vacuum (Fig. 4).

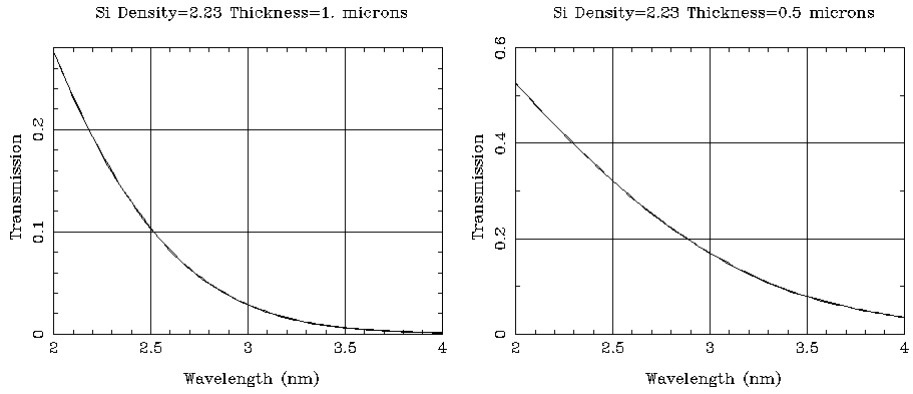

Fig. 3: *Transmission in Silicon for thickness $d = 1{\times}10^{-6}$ m and $d = 0.5{\times}10^{-6}$ m in water window region. [12]*

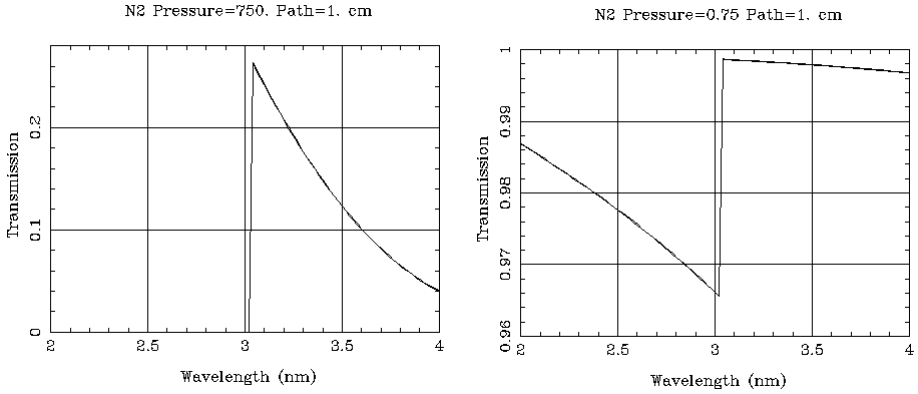

Fig. 4: *Transmission in Nitrogen for $p = 1$ bar and $p = 10^{-3}$ bar in water window region. [12]*

1.3 Plasma Radiation

Substances of all states emit electromagnetic waves, the formation of which is related to the disordered movement of electrically charged particles. Such radiation is referred to as heat radiation. The model of the absolutely black body and Wien's law are used to describe this radiation,

$$\lambda_{MAX} = \frac{b}{T}, \tag{1.4}$$

where the constant $b = 2.898 \times 10^{-3}$ m.K and T [K] is the thermodynamic temperature of the black body. As the temperature of the emitter increases, the maximum spectral density of the radiation intensity shifts to shorter wavelengths. The spectral density of the radiation intensity is given by

$$\mathrm{H}_\lambda = \frac{2\pi hc^2}{\lambda^2(e^{(hc/\lambda kT)} - 1)}, \tag{1.5}$$

where c is the speed of light, $k = 1.38 \times 10^{-23}$ J.K^{-4} is the Boltzman constant, T is the absolute temperature, h is the Planck constant and λ is the radiation wavelength.

If we want to obtain wavelengths of approximately 3 nm, we need to increase the temperature many times to increase the spectral density of the radiated energy. After substituting into the relation (1.4), we get the temperatures that need to be reached for the generation of required SXR radiation.

$$T = \frac{b}{\lambda_{MAX}} = \frac{2.898 \times 10^{-3}}{2.2 \times 10^{-9}} = 1.317 \times 10^6 \mathrm{K} \approx 113.4 \mathrm{eV} \tag{1.6}$$

Plasma radiation is composed of continuous and line wavelength spectrum. The line spectrum is the result of quantum transitions of electrons from higher to lower energy levels. The wavelengths of the spectral lines are described by the relation:

$$\lambda = \frac{hc}{(E_2 - E_1)}, \tag{1.7}$$

where E_2 is the upper level and E_1 is the lower level energy of atom.

All elements except H, He, Ar, Kr, Xe, F, Cl, Br, I, N, O, S, P, C, Se, and Hg have an ionization potential of less than 10 eV. Therefore, their excitatory potentials cannot exceed this value and lie predominantly in the range of 4 - 6 eV. For excitation energies E = 6.0 eV, the spectral lines will have $\lambda > 206.6$ nm according to the equation (1.7).

The resonant atomic lines of most elements consequently occur in the region above 200 nm. The width of the spectral line results from the properties of atom radiation and external conditions. The theoretical line width is in the range of 10^{-4} - 10^{-5} nm and does not depend on wavelength [36]. The real width tends to be wider. The Doppler extension of the line as a result of the thermal movement of glowing particles is given by:

$$\Delta\lambda = 7.2 \times 10^{-7} \lambda_0 \sqrt{\frac{T}{A}} \text{ [nm]}, \tag{1.8}$$

where A is atomic weight, λ_0 is wavelength and T is temperature. The Doppler extension is, therefore, greater for lighter elements and increases with temperature. In thermodynamic equilibrium, the concentration of particles with a certain excitation level is determined according to the Boltzmann equation:

$$N_m = N_0 \frac{g_m}{g_0} e^{-(E_m/kT)}, \tag{1.9}$$

where N_0 is the number of atoms or ions, g_m and g_0 are statistical weights of excited and ground level, E_m is excited energy level, k is Boltzmann's constant, and T is absolute temperature. The intensity of spectral line corresponding to the spontaneous transition of the excited atom or ion between the levels $m \to n$ results from the following relation:

$$I_{mn} = N_0 h\nu_{mn} P_{mn} \frac{g_m}{g_0} e^{-(E_m/kT)}, \tag{1.10}$$

where P_{mn} is the probability of transition (Einstein's coefficient for spontaneous emission).

As the temperature increases, the intensity of lines increases, but the degree of ionization also increases, which is manifested by the fact that the intensity of the line with rising temperature increases, reaches a maximum at a certain value and decreases again. The position of the maximum depends on the excitation energy of the line, the ionization potential of the element and the composition of plasma.

Although plasma can be formed from any gas, noble gasses are preferred. Moreover, their high ionizing energy values allow efficient ionization of most elements. For *water window* spectral range we have to choose gasses with corresponding properties:

- Nitrogen
- Argon
- Krypton
- Xenon

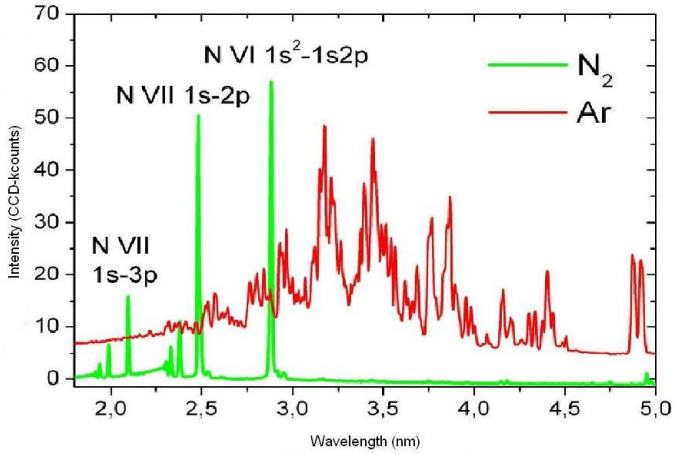

Fig. 5: *Radiation spectrum of Nitrogen and Argon in water window.*

1.4 Soft X-Ray Sources

Soft x-ray microscopy is based on highly chromatic diffractive optics. To reach the large number of photons required for high-resolution imaging, bright narrow bandwidth ($\Delta\lambda/\lambda < 1\ 500$) soft x-ray radiation is needed. Spectral brightness is usually defined as [photons/(s $\times$ srad $\times$ μm^2 $\times$ 0.1%BW)]. For pulsed sources it is more convenient to use photons per pulse and for line-emitting sources the bandwidth of a line is often chosen. Depending on the application, other aspects of the radiation may also be of importance, e.g., average output power, coherence, source size and emitted spectrum. Today there exist a number of source technologies for soft x-ray generation, each having their advantages and disadvantages and the development of new ones is quite intense. Figure 6 compares the spectral brightness for a selection of existing and future x-ray sources. This section gives a short description of the compact source technologies that are available for soft x-ray microscopy in *water window*.

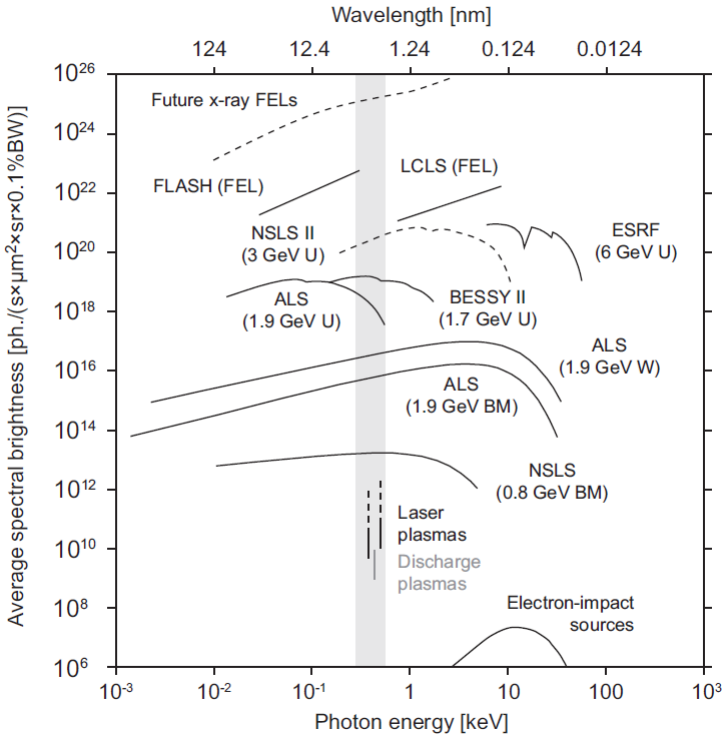

Fig. 6: *Comparison of radiation sources. The chart compares existing (solid lines) and planned (dashed lines) radiation sources. The water window is marked in grey. [34]*

1.4.1 Laser-Produced Plasma Sources

As an alternative to synchrotron radiation sources, we can use laser-produced plasma (LPP) sources. They produce soft x-rays at high spectral brightness and could be compact for laboratory experiments. The comprehensive theory is described in Refs. [2]. Here, we will use the approach of black-body radiation for description of basic properties.

The wavelength, for the emitted spectrum from a black-body with temperature T peaks, is given by Wien's displacement law:

$$\lambda_{peak} = \frac{2.898 \times 10^6}{T} \tag{1.11}$$

The temperature corresponding to soft x-rays is in order of $\sim 10^6$ K. To get such high temperatures we have to focus the high-power laser pulse into the target. The laser output should be around 10^{13} W/cm^3. Different experimental schemes are illustrated in Figure 7.

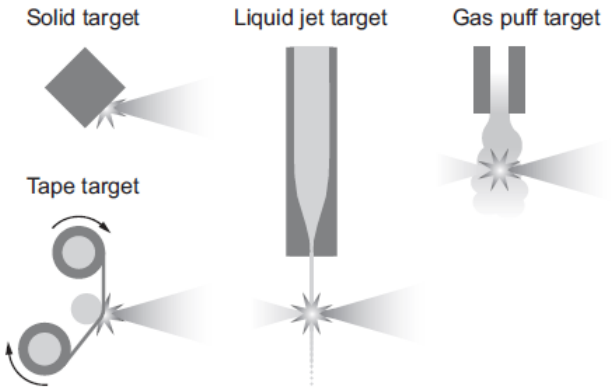

Fig. 7: *Laser plasma sources. Target types used for soft x-ray generation. [34].*

When the laser hits the target, plasma is formed from free electrons and ionized atoms. Due to inverse bremsstrahlung absorption plasma is heated and it starts expanding. An essential condition for the realization of the LPP source is to generate such a plasma, so that the necessary ions are present in sufficient quantities and that the upper levels of the selected quantum transitions would preferably be excited. Table 2 shows the ion overview that can be used for emission in *water window*.

Ion-type	**Ion**	**quantum transition**	λ **[nm]**
H-like	Li^{2+}	$n = 1 \rightarrow n = 2$	13.5
	B^{4+}	$n = 1 \rightarrow n = 2$	4.8
	C^{5+}	$n = 1 \rightarrow n = 2$	4.5
	aL^{12+}	$n = 2 \rightarrow n = 3$	3.8
He-like	N^{6+}	$1s2p4 \rightarrow 1s^2$	2.88

Table 2: *Ions, quantum transitions and wavelengths of SXR lasers*

1.4.2 Discharge Plasma Sources

High current pinching gas discharge in capillary may be used as an SXR source [6]. The formation of the plasma is described in detail in Ref. [37]. At the beginning of the discharge, the current flowing through the gas will create a low temperature plasma. The free charges of the plasma charges reduce the resistance and the discharge current quickly increases, inducing a strong magnetic field that pulls offaxis-moving charged particles towards the central axis. This compresses or "pinches" the plasma, thereby increasing the density and temperature to levels where soft x-rays are emitted. Pinch plasmas can be used for laboratory *water window* microscopy [38], but the source size is large, about 1 mm, and the brightness is about one order of magnitude lower than for LPPs [39], see Figure 6. Pinch-plasma sources have been commercially available for EUV radiation for years, and companies like NanoUV and Energetiq announced their availability for *water window* radiation. The technology developed by Energetiq circumvents a common problem with electrode erosion by generating the pinch-plasma via magnetic inductive coupling instead of electrodes.

Type	λ **[nm]**	Q_{euv} [ph/sr×pl]	**Source size**	**C [nF]**	**Ref.**
nitrogen	2.88	10^{12}	200 μm	13.5	Vrba, Zakharov, 2011, [6]
nitrogen	2 - 4	10^{12}	$<$ 1 mm	-	Energetiq, 2012, [40]
nitrogen	2.89	10^{12}	1.6 - 3.2	1.6	Wyndham, Favre, 2009, [41]

Table 3: *List of sources based on DPP in water window. C is capacity on the condensers.*

1.5 LLG SXR Source System

This part is focused on diagnostic and optimization of an SXR source that was bought from Laser-Laboratorium Göttingen e.V. (LLG) and has been operated in XUV Laboratory at Faculty of Biomedical Engineering, Czech Technical University in Prague.

Description of the SXR Source System

The SXR source system is composed of 2 parts - laser-produced plasma source that uses gas for generating radiation in *water window*; and interaction part. The LPP source is based on gas-puff target operates with Argon or Nitrogen as working gasses and an excitation Nd:YAG laser with focusing optics. Figure 8 shows the photo of the system and Fig. 9 shows the block diagram of the LPP source.

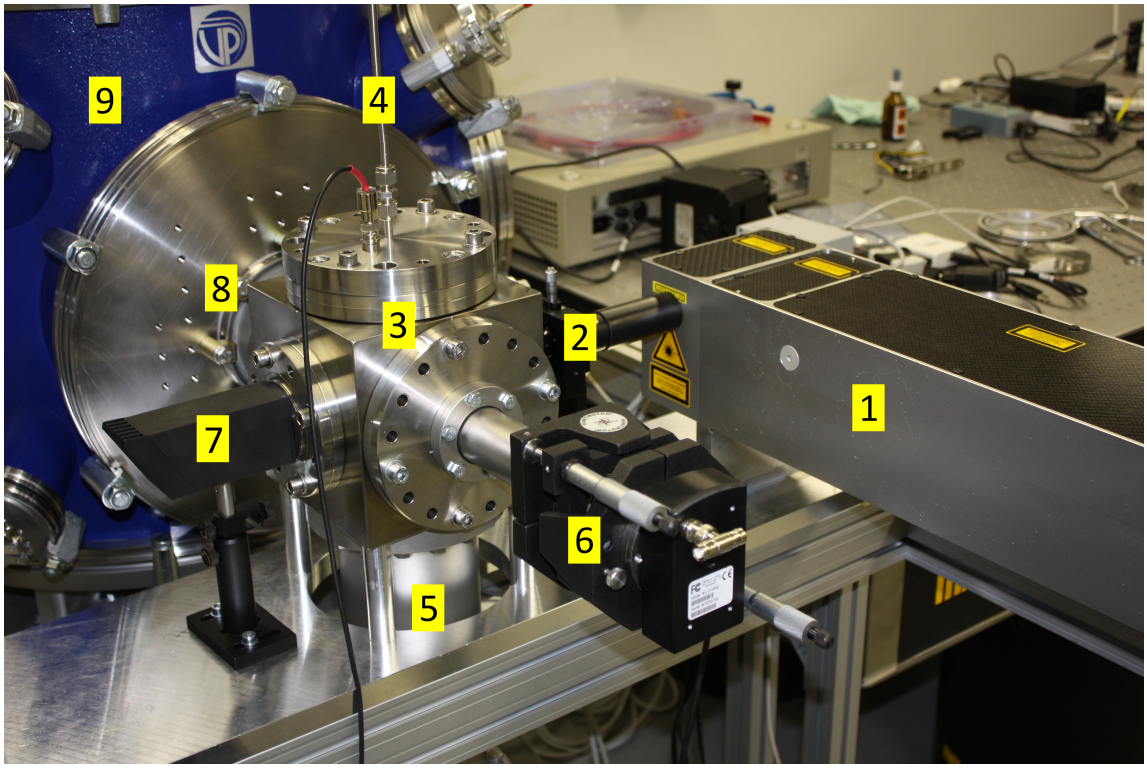

Fig. 8: *LLG SXR source. 1 - Nd:YAG laser, 2 - focusing lens, 3 - nozzle, 4 - valve, 5 - gas evacuation, 6 - LLG pinhole camera, 7 - black hole, 8 - photo-diode in vacuum chamber, 9 - interaction vacuum chamber. [27]*

Plasma is generated by focusing the infra-red Nd:YAG laser through a plan-convex lens with $f = 100$ mm in the gas-puff target (Fig. 10). Excitation laser works on

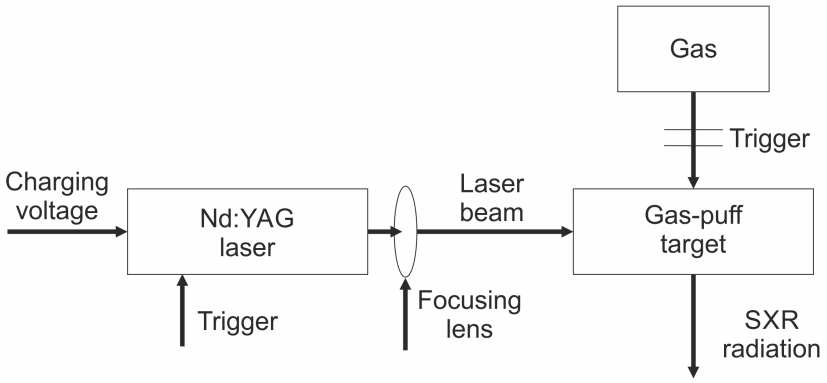

Fig. 9: *Block diagram of LLG SXR source.*

wavelength $\lambda = 1\ 064$ nm with energies E= <400-800> mJ [42]. The focal spot from the input lens has a diameter of about 60 μm. The operation density is higher than $4{\times}10^{12}$ W/cm^2. Output energy from the SXR source is measured by AXUV20HS1 photo-diode [43] 303 mm far from the focal point. The Ti filter (Figure 11) and iris with $d_{IR} = 1$ mm is placed before the photo-diode. With this simple arrangement, we measure the output energy and we are able to see the plasma spacial distribution. Figure 12 shows incurred plasma with his spacial distribution of luminous intensity taken by 30μm pinhole camera with 400 nm Ti filter and CCD (724×568 px).

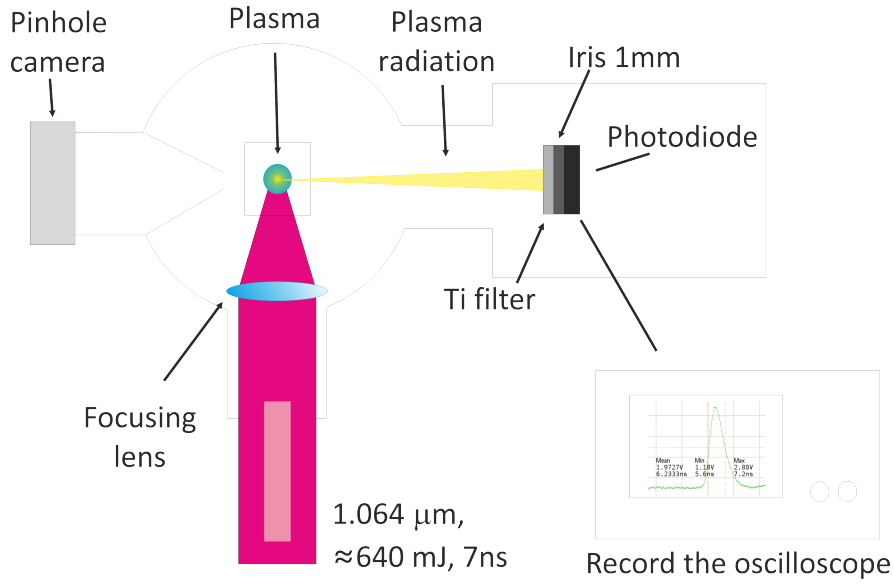

Fig. 10: *Experimental arrangement. Output energy from SXR source was measured by AXUV photo-diode 303 mm far from plasma after the Ti filter.*

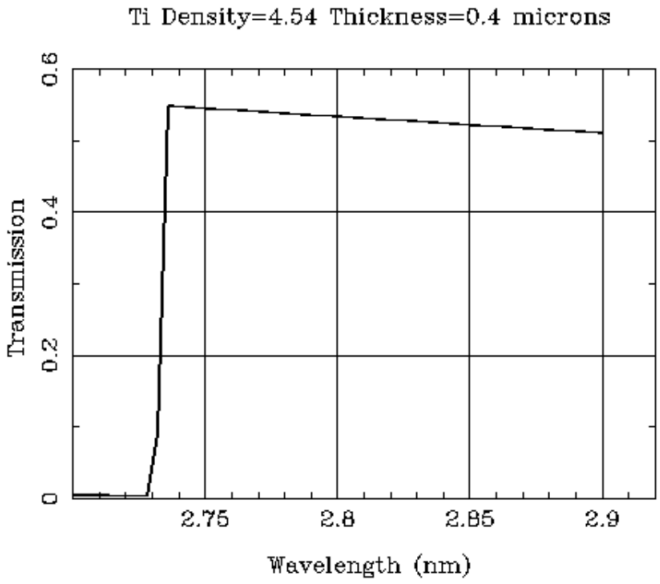

Fig. 11: *Transmission of Ti filter d = 400 nm thin. [12]*

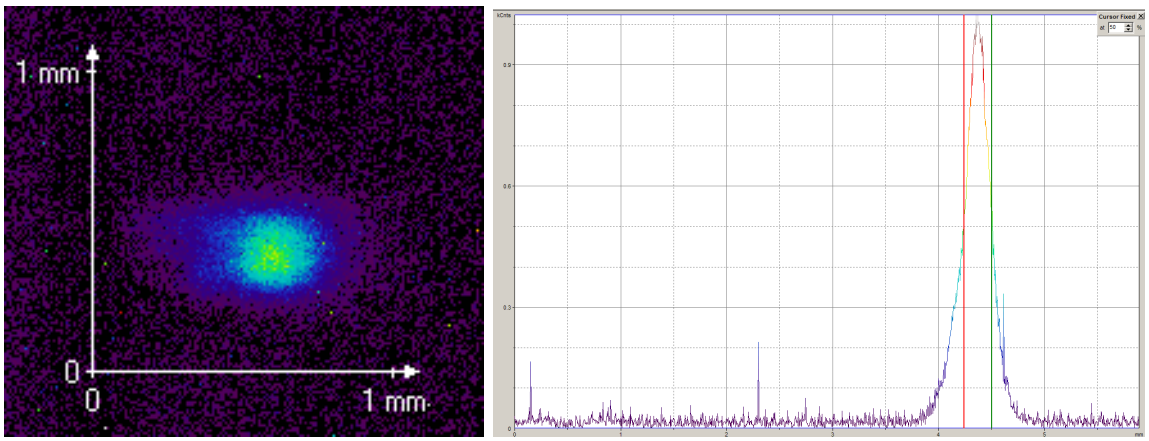

(a) (b)

Fig. 12: *(a) Plasma taken by LLG 30μm pinhole camera with 400 nm Ti filter and CCD (724×568 px), (b) spacial distribution of luminous intensity. Δz = 460 μm, p = 12 bar, f = 2 Hz, delay t = 1 050 μs.*

1.5.1 Optimization Function

The goal is to achieve the most photons/srad in optimal arrangement to comparison with other sources that were mention in chapter 1.4. For fulfilment of this goal is important find all parameters that influence the input radiation and choose the best combination of them.

We can define the optimization function $F(E_{out}) = F(\lambda, E_{in}, f, \Delta t, h, \rho, \Delta z, p_{in}, p_b)$. List of parameters in the function $F(E_{out})$:

- Excitation laser wavelength λ
- Excitation laser energy E_{in}
- Laser repetitive frequency f
- Time delay between valve opening and excitation laser pulse Δt
- Depth of field of Nd:YAG laser in the focal plane h
- Gas density in gas-puff target ρ
- Distance of the focal point from the nozzle Δz
- Input gas pressure p_{in}
- Background pressure in vacuum chamber p_b

A preliminary study of some parameters was done in the diploma thesis [27].

Next parameters that influence the plasma generation are nozzle size and profile and working gas. In chapter 1.4.1 we introduce the elements that could be used in the SXR source. In a case of SXR source based on gas-puff target the Argon, Krypton, Nitrogen, and Xenon are mostly used according to the selected emission bandwidth. Nitrogen has the narrow emissions line at $\lambda = 2.88$ nm. Noble gasses are used due to high particle density and wide spectrum. The spectrums and densities for each gas are shown and more discussed in chapters 1.3 and 4.1.1.

1.6 Overview of Biological Samples

The SXR microscopes are developed for imaging small object, especially biological samples. In *water window* region (2.34 - 4.4 nm) is big difference between protein and water transmission. Nearly all SXR radiation is absorbed in proteins and on the other hand water is transparent. This effect allows to image small live structures in the water environment. Wavelength allowed us also have the ratio in tens nm. Unfortunately, there in problem with the samples. Most microscopes work with a brightness of 10^{11} photons/srad. It could be enough for imaging the wet samples if there is not a big attenuation in atmosphere (especially due to Nitrogen). From this reason the SXR source works with evacuated chambers. But it is problem for live cells. To date, this problem has not been reliably solved and most microscopes use dried or frozen specimens.

We present an overview of mostly used biological samples and their use in SXR microscopy.

- Dehydrated COS-7 cells [44]
- Spironucleus salmonicida [45]
- Diatoms [34]
- Yeast[46]
- Eukaryotic cells [47]
- Chlorella sorokiniana [48]
- Microcystis wesenbergii [49]
- A431 human epithelial cells [50]
- Frozen 3T3 cells [51]
- CT 26 fibroblasts [21]

For samples preparation very often are used methods of freeze-drying, freezing under high pressure or dehydration that was used for our samples. By freeze-drying it may damage the membrane if the exact procedure is not followed. By freezing under high

pressure sample is allowed to grow on the membrane and is subsequently frozen inside the chamber. This method is suitable for shorter exposure (sample damage was reported several times in literature). Dehydration is done by series of ethanol-distilled water washes.

2 Aim of Dissertation

The aim of my thesis was to optimize the source of SXR radiation for biological samples imaging, which is located in the XUV laboratory at the FBME CTU. Thanks to the short wavelength, we are able to achieve image resolution below 100 nm, which helps to detect changes at the level of cellular organelles.

Unfortunately, SXR radiation has a high attenuation when passing through almost all materials, resulting in a rapid decrease in the intensity of output radiation. When imaging, we are also limiter by sensitivity of CCD detector. This implies our efforts to maximize the intensity of output radiation from the plasma source.

Our SXR source works on the principle of Laser-produced plasma, specifically with a gas target heated by IR laser. Nitrogen and Argon are used as working gasses. Increasing the intensity of output radiation can be achieved either by changing the laser tuning or by changing the gas-puff target.

My assignment was to formulate an optimization function and find correlation of the individual parameters of the whole system to achieve the highest output energy in a single shot. From a series of measurements, we gradually found out the most important parameters affecting the whole system. Specifically, it was spacial distribution of the target mass density ρ, the distance Δz of the target from orifice of the nozzle and the time delay Δt between gas injection and the opening of excitation laser. Based on the knowledge of these parameters and system behaviour, the optimal settings for current operation of the SXR source was designed. In addition, creation of a target models involving gas expansion through nozzle was suggested. This model was created in 2D RMHD code Zstar, which was used for this purpose for the first time.

The validity of the model should be confirmed by comparison of evaluated data with experimental data. To this purpose it was decided to measure the spatial distribution of the gas density using a shadowgraph experiment.

The laboratory should have been also prepared to work with biological cells. I did a literature research of the biological samples used so far and their method of preparation for environment of vacuum chamber while maximizing their internal structure.

To preliminary experiments were prepared at FBME with dehydrated CT 26 fibroblasts and for the first time they were imaged during experiments in our collaborating laboratory of Laser-Matter Interaction Group, MUT in Warsaw.

3 LLG SXR Source System Diagnostic

In this chapter, we will gradually focus on the individual parameters of optimization function $F(E_{out})$ that was delineate in chapter 1.5.1.

Nd:YAG Laser Diagnostic

The gas-puff target is excited by Nd:YAG laser Innolas "Spitlight 600" on the wavelength $\lambda = 1\ 064$ nm. That is the first parameter of $F(E_{out})$ and it will be static. According to technical documentation [42] we can operate the laser in the output energy range from 400 to 800 mJ due to the variation of excitation charging. The determining laser parameters are:

- output laser energy
- pulse duration
- stability of system

We measured the dependence of an output laser energy on the excitation charging. Output energy was measured with J25LP-YAG detector and TDS 3052B oscilloscope. The experimental set-up is in Figure 13.

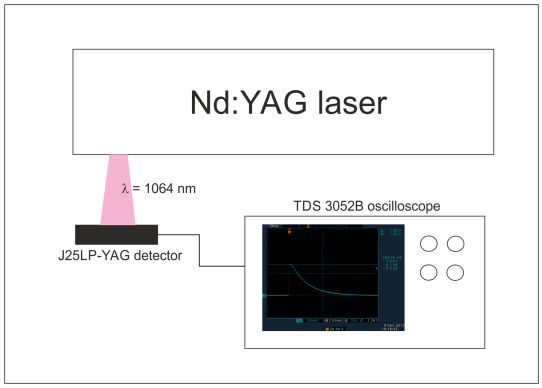

Fig. 13: *Schema of output Nd:YAG laser energy measurement.*

Figure 14(a) shows a linear trend of Nd:YAG laser output energy. The repetition rate was $f = 2$ Hz and the values we have taken as average from 500 shots for each voltage. We also measured the laser stability from the most commonly used voltage. This measurement was done for repetition rate $f = 1$ Hz and, $f = 2$ Hz - standard settings. The output energy was similar for both rates (Fig. 14(b)).

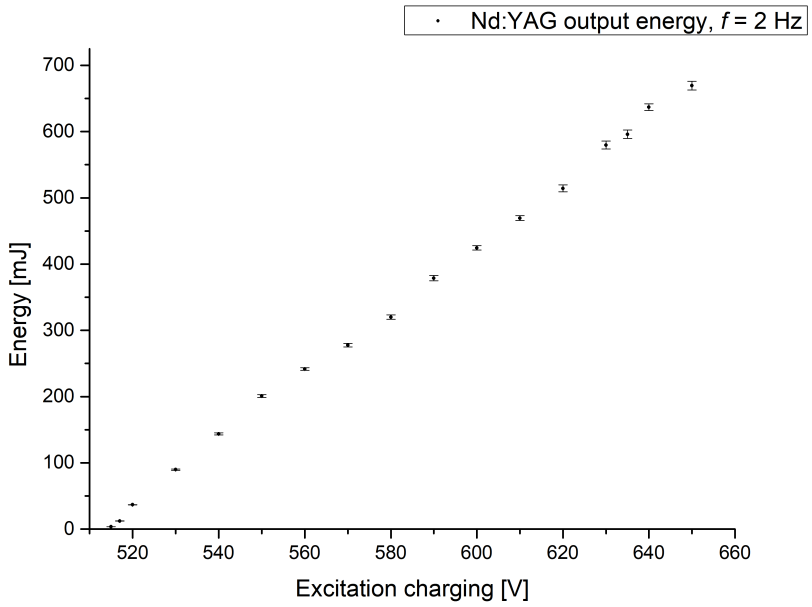

(a)

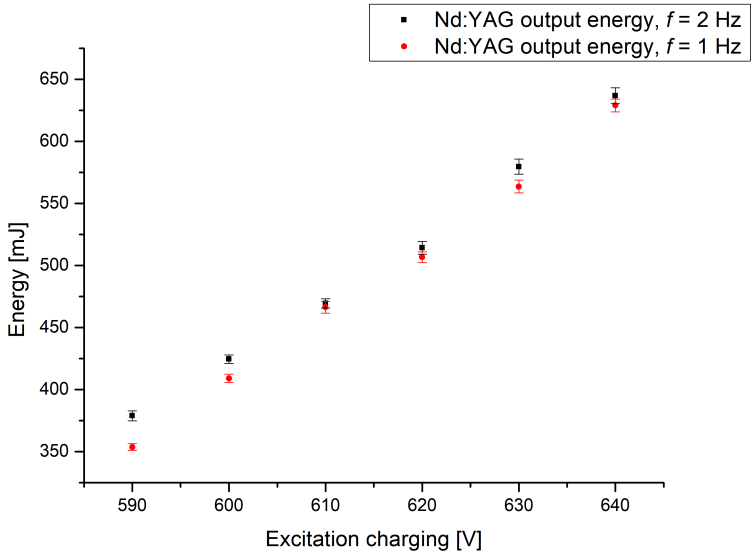

(b)

Fig. 14: *a) Dependence of output laser energy on excitation charging from threshold generation to its maximum and b) detail for 2 different repetition rate in the field of interest.*

The next parameter that affects also the output energy is Nd:YAG laser pulse duration. It depends on laser excitation charging as is shown in Figure 15. For higher excitation charging we get shorter pulse witch means that the power of the laser radiation increase.

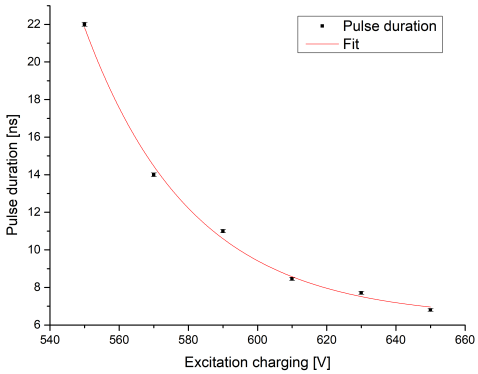

(a)

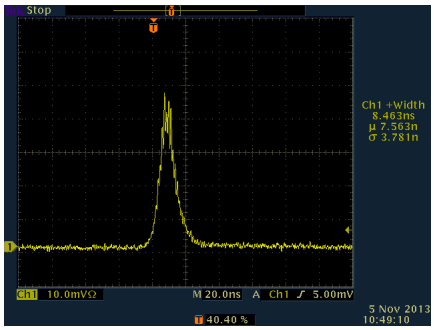

(b)

Fig. 15: *a) Dependence of Nd:YAG laser pulse length on laser voltage. b) Profile of Nd:YAG laser radiation for $U = 620$ V.*

The standard deviation for all measurement of laser energy and pulse duration is under 5 % that shows a very stable system. This information can help us with optimization. We need the most power that we can get from the laser for plasma creation. If we fix parameter E_{in}, we can simplify the optimization function. Table 4 shows the values of laser power input in one shot.

Excitation charging [V]	**Output energy** E_{in} **[mJ]**	**Pulse duration [nm]**	P **[MJ.s^{-1}]**
550	200.8	22	9.13
570	277.5	14	19.83
590	378.7	11	34.43
610	469.3	8.46	55.48
630	579.5	7.71	75.17
650	669.3	6.8	98.44

Table 4: *Table of laser parameters. Excitation charging is given firmly. Output energy and Pulse duration were measured and P was counted. [52]*

The energy of excitation laser is defined by laser type. It can be changed only in specific region by changing laser excitation charging.

Repetitive Frequency f

The SXR source operates with 3 repetitive frequency $f = 0.5;\ 1;\ 2$ Hz. This frequency has no influence on laser radiation but it can affect the plasma spot. Due to the inlet of gas into the vacuum chamber, pressure changes in the apparatus occur. Using a constant repetition rate of $f = 2$ Hz, with which most of our measurements were done, this parameter could be neglected. However, when using the SXR source only in single-shot mode, it is necessary to check whether, for example, the output energy variation or other changes are occurring.

First, we changed the laser repetition rate successively and recorded the course of pressure changes in the vacuum chamber, as shown in Figure 16. The pressure development after exhaustion to the initial value of $p = 0.3{\times}10^{-4}$ mbar and subsequent start of the gas injection. Gradually we changed the laser frequency to $f = 2$ Hz, $f = 1$ Hz and $f = 0.5$ Hz. The pressure was measured using a Pfeiffer Vacuum MPT 100.

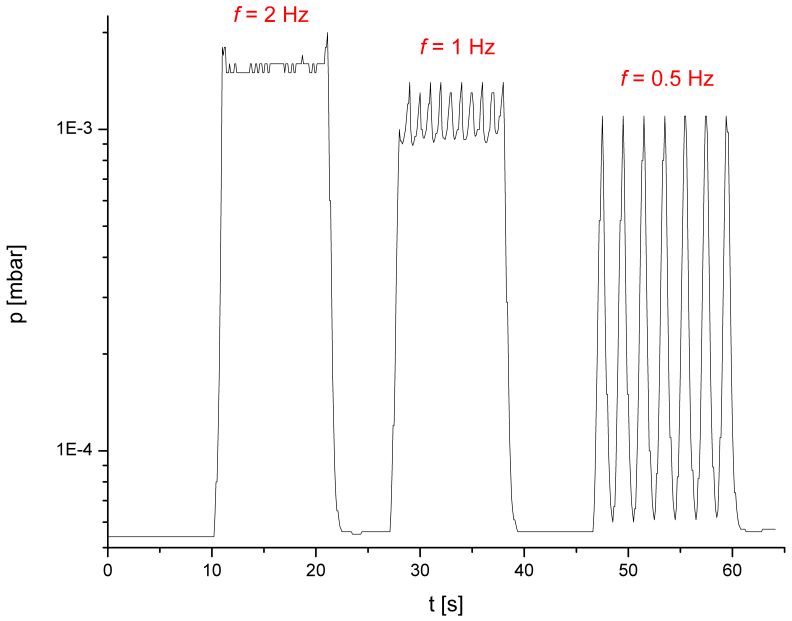

Fig. 16: *Dependence of pressure on time at different laser repetition rate and simultaneous injection of Argon into the vacuum chamber.*

From Figure 16 it can be seen that at a lower repetition rate, we are always able to pump the vacuum chamber to the original pressure of $p_b = 0.3{\times}10^{-4}$mbar. These results can have an effect on plasma generation and output radiation (Figure 4). This

measurements closely related to background pressure in vacuum chamber p_b and it will be detailed discussed in chapter 4.2.2.

Time Delay Δt Between Valve Opening and Excitation Laser Pulse

To plasma creation, we need to connect the Nd:YAG and the gas-puff target. First we start creating the gas-puff target and after a time delay the laser open and shots into the target. The manual recommends gas pulse duration 800 - 900 μs. We studied an synchronization interval Δt = <900;1400> μs to find the best time delay Δt between valve opening and laser action.

The excitation Nd: YAG laser and the nozzle that injects gas into the vacuum chamber are electronically controlled so that the delay between the laser shot and the formation of the gaseous target can be precisely adjusted. This delay is done by TriggerDAC software supplied by a producer. For an ideal gain from an SXR source, a time delay range of 900 μs to 1200 μs has been defined. We have shifted this interval up to 1400μs. We investigated the effect of these delays on the output radiation and its stability for several series of measurements. Here we present results for two excitation charging and two Nitrogen input pressure (Fig. 17).

These measurements show that the time delay is a very variable parameter. For the setting of each parameter, we have measured the entire output radiation/delay curve. The shape of the resulting output energy curve varies depending on working gas, input pressure, excitation charging and focus position. As it turned out, this curve does not have the same shape for different settings. We have therefore studied the shape of this curve while retaining one parameter. We operate the system in range Δt = <1050;1200> μs. It is always necessary to select the appropriate delay, which guarantees a high plasma output radiation for each measurement.

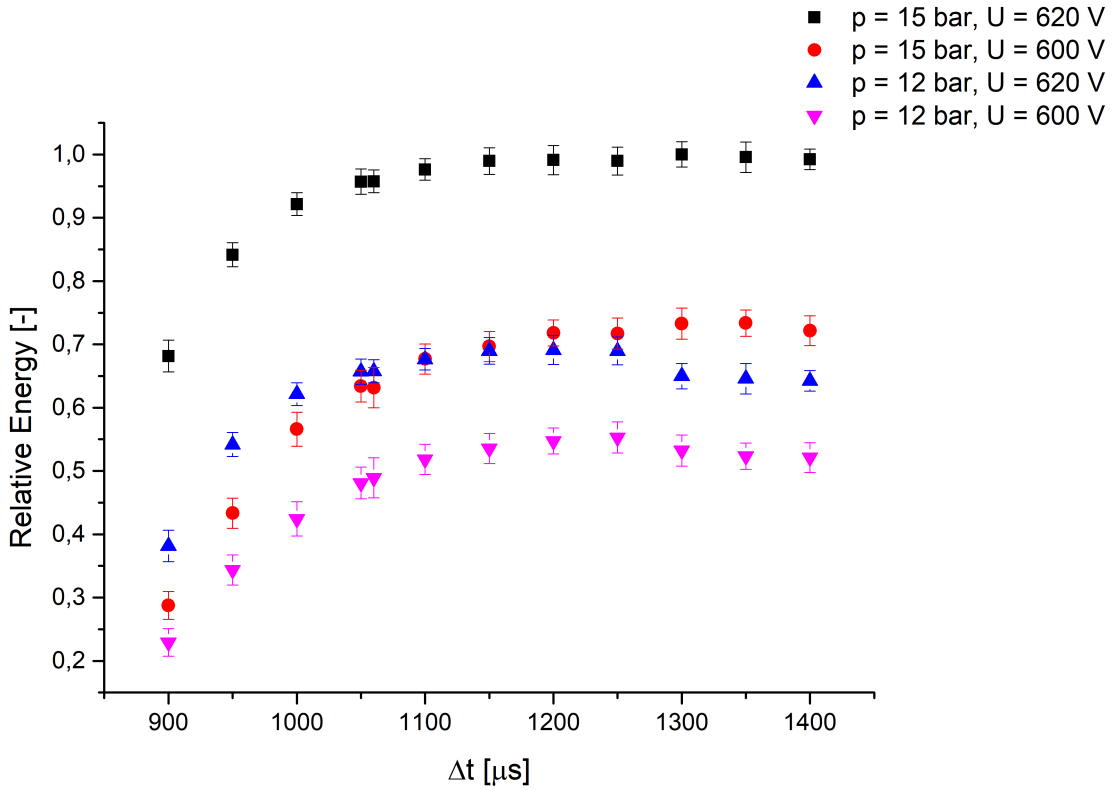

Fig. 17: *Relative energy dependence on time delay* Δt *for excitation charging* $U = 600\,V$ *and* $U = 620\,V$. *Nitrogen input pressures* $p_{in} = 12$ *bar and* $p_{in} = 15$ *bar.*

Depth of Field of Nd:YAG in the Focal Plane h

For plasma creation, it is also very important focusing the Nd:YAG laser through the lens into the gas-puff target in a vacuum chamber. The laser is focused by a plan-convex lens ($f = 100$ nm). The laser focus has a diameter of about 60 μm. Schema of gas-puff target and laser focusing lens is in Fig. 18.

We studied the plasma radiation and changes of the plasma energy spatial distribution depending on the depth of field of Nd:YAG in the focal plane h. We fixed the input parameters that are in Table 5. For measurement, we used AXUV photodiode (type AXUV100HYB1/V) [43], which is able to detect radiation in the *water window* region. The position of the focus was determined using a pinhole camera. The photodiode was located 303 mm from the focus and was preceded by an iris with a diameter of $d_{IR} = 1$ mm and a titan filter to remove unwanted wavelengths. The focus can be changed in the direction in axes x and z, as shown in Figure 18. Δz indicates the

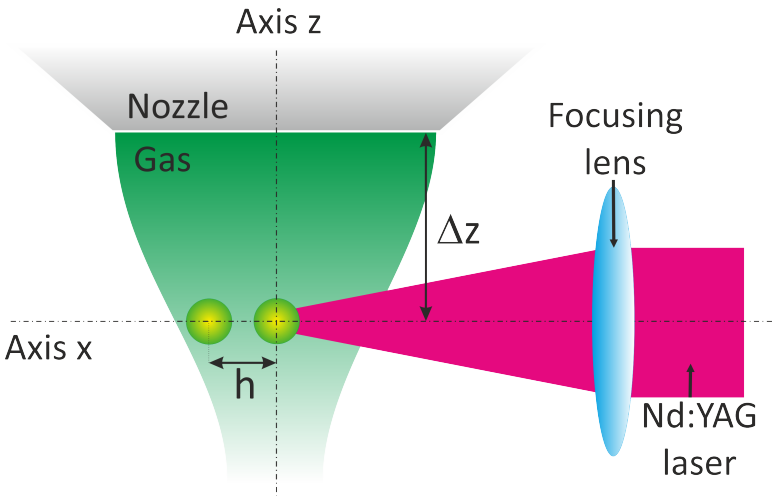

Fig. 18: *Geometry of interaction area. Green - gas-puff target, yellow-green - plasma spot, Δz - distance of the focal point from the nozzle, h - depth of field in the focal plane.*

distance from the nozzle and h the focus depth.

	Set 1	**Set 2**
p_{in}	12 bar	15 bar
Δz	0.5 mm	0.5 mm
U	600 V	600 V
f	2 Hz	2 Hz
Δt	1050 μs	1050 μs

Table 5: *Table of 2 sets input parameters for measuring the depth of field h.*

Figure 19 shows the relative intensity of plasma radiation depending on the depth of field change. We studied distance $\pm$ 1 mm on the axis x from the x-z intersection. Record from camera depicted in Figure 20 shows extreme positions of the interval and plasma spot recorded with the spacial distribution of luminous intensity is shown in Figure 12. The output radiation does not show major changes, even when the other parameters change, and we can simplify the $F(E_{out})$ in parameter h.

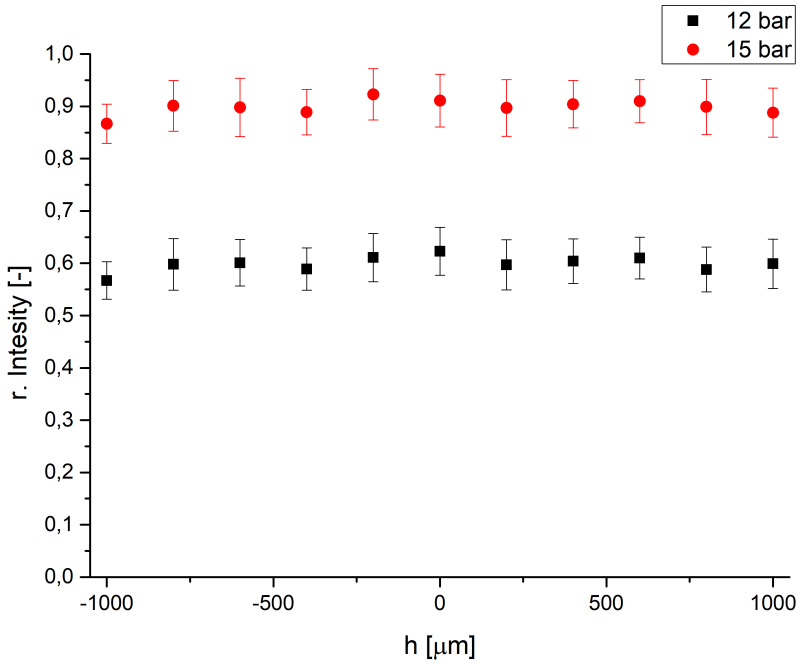

Fig. 19: *The plasma radiation relative Intensity depending on the depth of field change.*

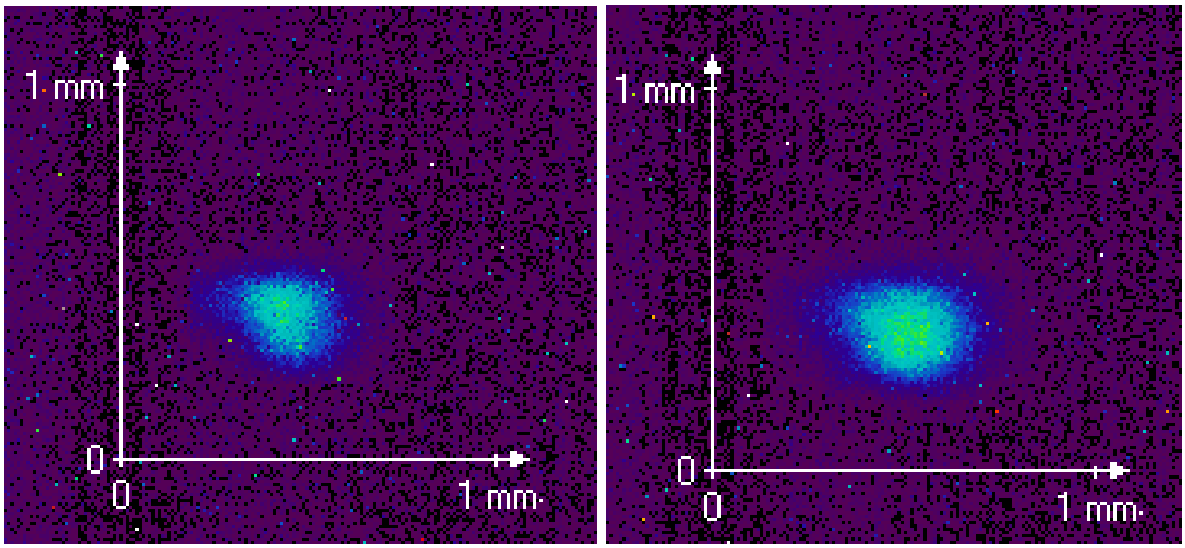

(a) h = -1mm (b) h = +1mm

Fig. 20: *Radiation from plasma spot ± 1 mm on the axis x from the x-z intersection. Input parameters p = 12 bar, d = 500 µm, f = 2 Hz, t = 1 050 µs.*

Input and Background Gas Pressures p_{in} and p_b

According to the SXR source manual, plasma is generated from $p = 5$ bar and the intensity increase linearly until $p = 40$ bar. Then the system is saturated and the output energy does not change [42].

In our SXR source system, the pressure works in range 5 - 15 bar because of the technical solution of the valve. The piezoelectric valve does not work correctly over $p = 15$ bar. If we operate the valve in the standard regime, the gas pressure closes the piezoelectric element that will not successively open for pressures over 15 bar. This can be fixed by adjusting the valve. But in this case, the valve does not lie on the nozzle and working gas flows into the vacuum chamber even if the valve should be closed. Due to this, the background pressure in the vacuum chamber increase and change the parameters of the whole system. We recommended the valve change for future upgrade.

For better clarity the parameters p_{in}, ρ, Δz and p_b are discussed in chapter 4.

4 Gas-puff Target Investigation

The gas-puff target is formed by pulse injection of a gas into vacuum through an electromagnetic valve synchronized with an irradiating laser pulse. I studied the gas profile and the density into focal plane where the laser is focused. I devoted experiments and simulations for future use of SXR sources system.

Nozzle Diagnostic

The nozzle is 1 mm high and has a conical shape as is shown in Fig. 21. It is made from wolfram. The focal spot where we are focusing the laser should be 0.5 mm far from the nozzle (listed in manual). Unfortunately, due to the small distance, we ablate the nozzle each time when the plasma is created. The detail in Figure 22 shows how the nozzle is damaged. This has an important influence on system parameters and optimization function.

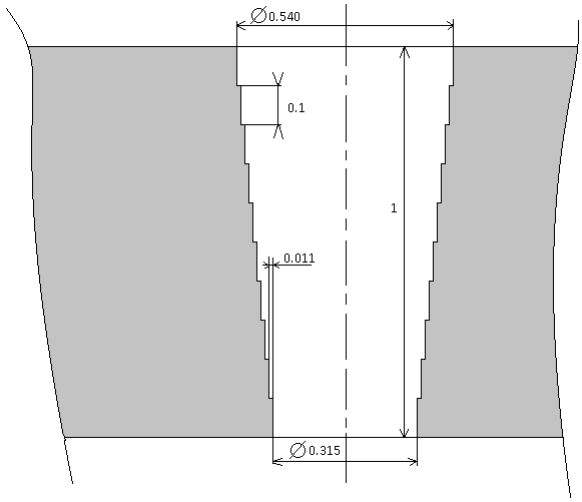

Fig. 21: *Profile of the nozzle in our SXR source system.*

To maintain the nozzle it would be appropriate to move the gas-puff target to a distance farther than 0.5 mm. We measured the dependence of plasma radiation on the distance Δz from the nozzle. The results are summarized in Figure 23.

Fig. 22: *Picture of the nozzle in SXR source system in XUV Laboratory at FBME, CTU in Prague. On left side new nozzle in a holder is depicted, on the right side is the detail of nozzle after 2000 shots.*

As we can see the plasma radiation rapidly decrease and it also depends on input pressure. This is closely related to the drop in mass density in the gas-puff target. Here we demonstrate that for the smaller distance the radiation increase. On the other hand, there is greater damage to the nozzle and system instability. A detailed investigation of mass density is in chapter 4.1.1.

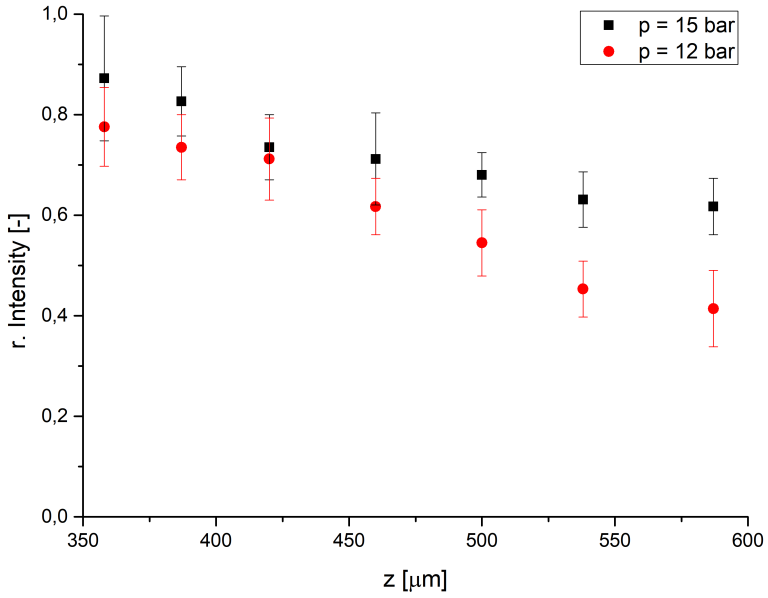

Fig. 23: *Relative intensity of plasma emission for $p = 12$ bar and $p = 15$ bar, $f = 0.5$ Hz, $\Delta t = 1.1$ ms.*

As we mentioned in chapter 3 (Measurement of Δt) the output radiation depends on time delay Δt between valve opening and excitation laser pulse. Due to the strong influence of parameter Δt on the resulting optimization function $F(E_{out})$, we measured the dependence of output intensity from the plasma spot on the chosen time delay for two different pressures and two positions Δz. We have standardized the resulting values for a clearer comparison. The highest value obtained from this series of measurements corresponds to 1. As we can see in Figure 24, relative intensity decrease with rising Δz for pressure $p_{in} = 12$ bar and $p_{in} = 15$ bar. An important result is that for a lower input pressure p_{in} a higher intensity is achieved with a lower time delay Δt, in contrast to an input pressure $p_{in} = 15$ bar.

As is seen from these results changes in mass density are very important for output radiation. I studied it via measurements and simulations. The obtained data were compared and I also performed simulations of new possibilities to increase particle density in gas-puff target.

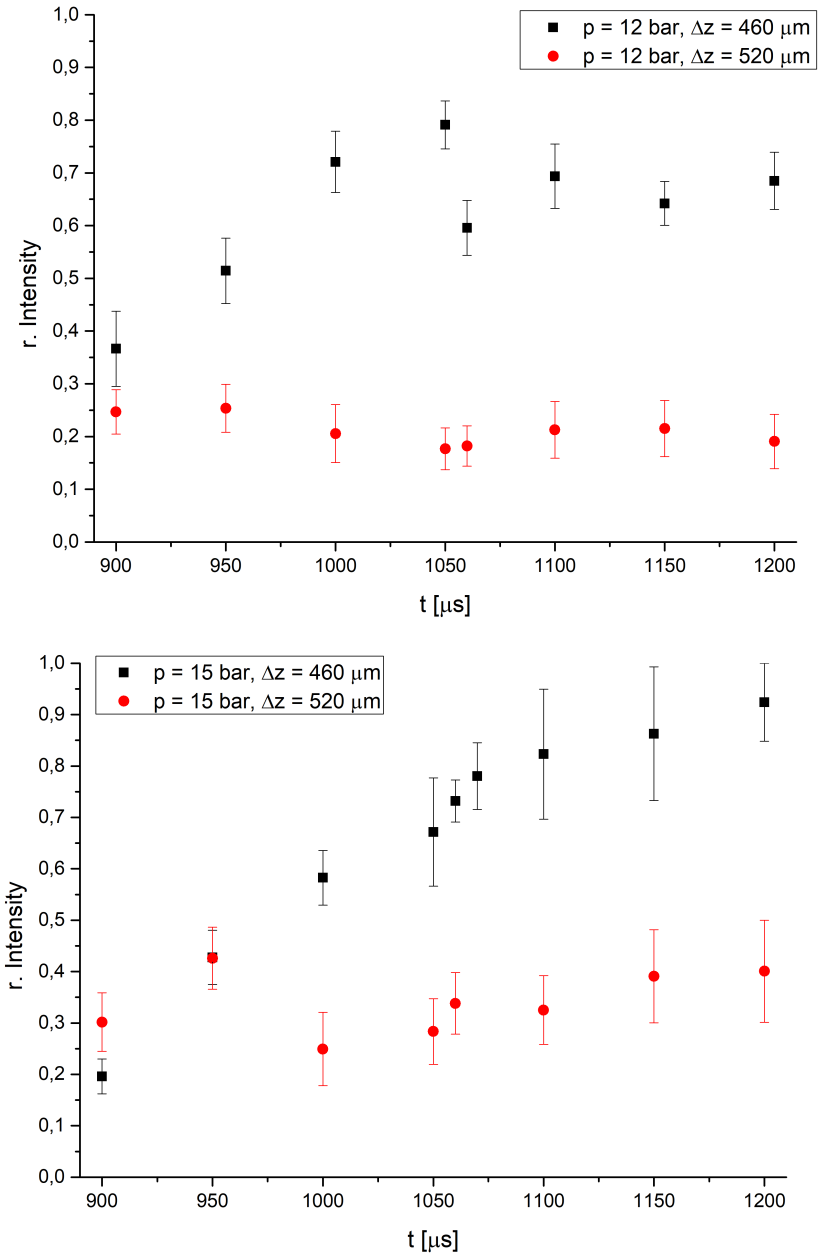

Fig. 24: *Dependence of relative intensity of plasma radiation on time delay* Δt *for an input pressure* $p_{in} = 12$ *bar and* $p_{in} = 15$ *bar.*

4.1 Shadowgraphy

4.1.1 Measurements of Mass Density in Gas-puff Target

Our SXR source was designed in Laser Laboratory Goettingen [53, 54]. The simplified scheme of the nozzle and gas-puff target is shown in Fig. 25. A single-stream supersonic nozzle forms the gas-puff target in the evacuated vacuum chamber.

The nozzle is a conical hole in a metal plate, located above a high-pressure reservoir and an evacuated space above the nozzle. At the beginning of the experiment, the gas pressure in the reservoir is increased almost immediately. The gas flows through the nozzle by supersonic speed. A variable gaseous target is formed above the nozzle, having in principle the cylindrical symmetry.

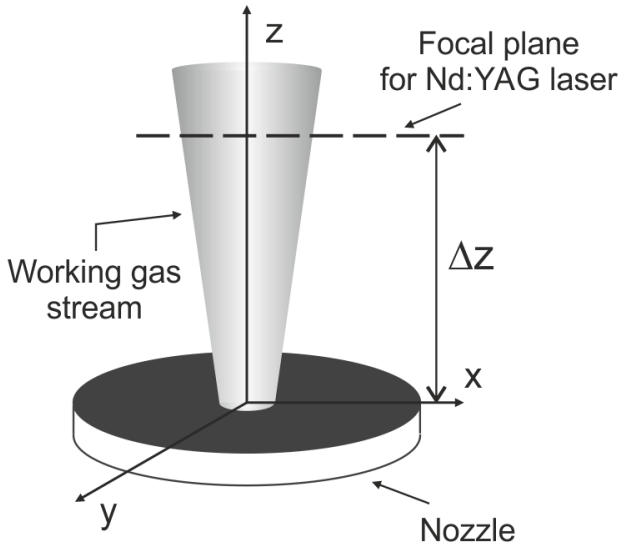

Fig. 25: *Scheme of gas–puff target.*

For our purpose, it is important to know especially the density of the target at time when the laser is fired and at the place, where the laser beam hits the target, i.e. at a distance Δz from the nozzle.

As we show above the mass density ρ is a key parameter for plasma creation and output radiation. We focused on the study of gas flow from the nozzle for different gasses and pressures and also on the changes of gas-puff target in relation to the ablation of the nozzle.

Arrangement of the Experiment

The setup of the experiment is shown in Figure 26. The gas-puff target was exposed to extreme UV radiation generated using a laser-plasma x-ray source. The investigated gas-puff target was located 640 mm away from the laser-plasma source ($\lambda = 13.5$ nm) and 155 mm from the CCD detector, all of them placed inside a vacuum chamber. Using another laser-plasma source means that all other parameters of $F(E_{out})$ have no influence on the results. This radiography was taken at time delay Δt_R, which corresponds to the time difference between opening the valve (moment of filling the reservoir) and time of exposure, which coincides with the time of plasma source emission, given by Nd:YAG laser shot. The gas-puff targets were backlit with EUV radiation. We get the shadowgraph that was here discoloured for better viewing.

The source of EUV radiation was laser-plasma created by Nd:YAG laser ($\lambda = 1064$ nm, $E = 450$ mJ) in N/He double gas-puff, then transmitted through the set of self-standing X-ray filters composed from 20 mm thick Si and 10 mm thick Be foils and reflective Si/Mo mirror to get the wavelength of 13 nm. The CCD camera used was M25 X-Vision Rigaku, 512 $\times$ 512 square pixels (24 μm), cooled by the Peltier element. The method was described in [55]. Argon, Krypton, Nitrogen, and Xenon gas-puff targets were studied. The CCD detector was exposed one time with the x-ray pulse.

The experiments were performed on another SXR source in the cooperating laboratory of Laser-Matter Interaction Group, Institute of Optoelectronics, The Military University of Technology in Warsaw [56].

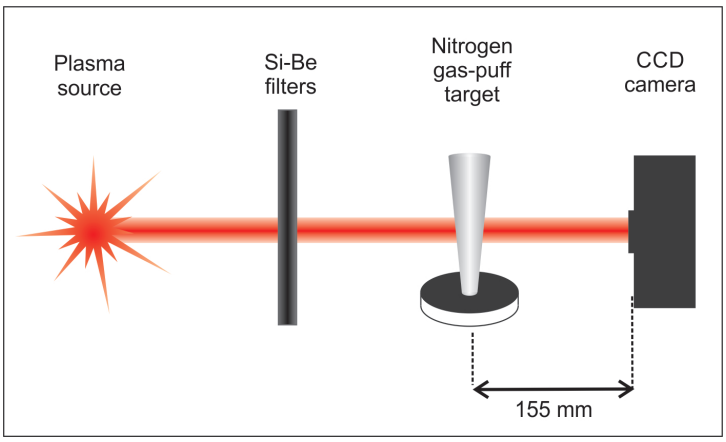

Fig. 26: *Principle scheme of the radiography experiment.*

Methodology

The scheme of gas-puff target is depicted in Figure 25. Δz is the distance of gas-puff target from the nozzle. The gas-puff target has cylindrical symmetry. The axis of symmetry coincides with coordinate z. For assessment of the spatial distribution of working gas mass density $\rho(x, y, z)$, we record the shadowgraph of the gas stream in the y-direction (perpendicular to the axis of symmetry z). Resulting x-z dependence of object radiography is determined by transmittance $T(x, z)$:

$$T\left(x,z\right) = e^{-\mu \int_N \rho(x,y,z)dy} \tag{4.1}$$

where μ is the gas absorption cross-section. Values for specific gasses are in Table 6.

Gas	μ **[cm^2/g]**
Nitrogen	5.3176×10^4
Argon	2.0948×10^4
Krypton	1.6544×10^4
Xenon	1.1428×10^5

Table 6: *Value of photo-absorption cross-sections for λ= 13.5 nm. [12]*

The mass density ρ is most important at the distance $\Delta z = 500$ μm from the nozzle where the laser beam is focused. Transmissivity is function of x only:

$$T\left(x,z\right) = e^{-\mu \int_{-y}^{y} \rho(x,y,\Delta z)dy} \tag{4.2}$$

If we assume cylindrical symmetry (Fig. 27) and the homogeneous gas density $\rho(r, \Delta z) = \rho_0(\Delta z)$ for $r < r_0$, otherwise $\rho(r, \Delta z) = 0$, we get trajectory length $\Delta y = \sqrt{r_0^2 - x^2}$.

The expression 4.2 can be rewritten as:

$$\begin{aligned} T_H\left(x,\Delta z\right) &= e^{-\mu\rho_0 \cdot 2 \cdot \sqrt{r_0^2-x^2}} \quad \text{for} \quad \rho < \rho_0\left(\Delta z\right) \\ &= 1 \qquad\qquad\qquad\quad \text{for} \quad \rho \geq \rho_0\left(\Delta z\right) \end{aligned} \tag{4.3}$$

If we assume that gas density profile is Gaussian, $\rho\left(r,\Delta z\right) = \rho_0 \cdot e^{-\frac{r^2}{2\sigma^2}}$ we get:

$$T_G\left(x,\Delta z\right) = e^{-\mu \int_{-\infty}^{\infty} \rho_0 \cdot e^{-\frac{(x^2+y^2)}{2\sigma^2}} dy} \tag{4.4}$$

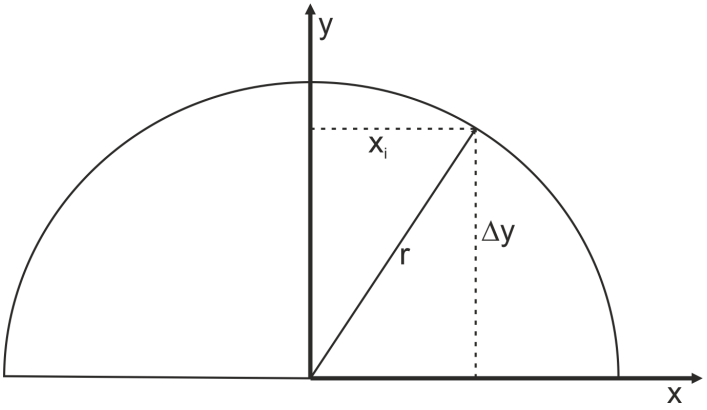

Fig. 27: *Cylindrical symmetry geometry.*

where σ is parameter of Gaussian function. After integration we get:

$$T_G\left(x, \Delta z\right) = e^{-\mu\rho_0\sigma\sqrt{2\pi}\cdot e^{-\frac{x^2}{2\sigma^2}}} \tag{4.5}$$

$$\ln T_G\left(x, \Delta z\right) = -\mu\rho_0\sigma\sqrt{2\pi}\cdot e^{-\frac{x^2}{2\sigma^2}} \tag{4.6}$$

From this equation the mass density is:

$$\rho_0\left(\Delta z\right) = -\frac{\ln T_G\left(x, \Delta z\right)}{\mu\sigma\sqrt{2\pi}}\cdot e^{\frac{x^2}{2\sigma^2}}. \tag{4.7}$$

The molecular (atom) density N at the axis of the nozzle at the selected distances $\Delta z = 500$ μm or $\Delta z = 1$ mm was estimated using the formula:

$$N = \rho_0(\Delta z)\frac{N_A}{M_r} \tag{4.8}$$

where N_A is Avogadro's number $N_A = 6.02\times10^{23}$ mol^{-1}, M_r is molecular weight.

Results for New Nozzle

We studied the new single-stream nozzle used in our SXR source system. The spatial distribution of the energy of monochromatic radiation transmitted through our gas-puff target in the proximity exposure is shown in Figure 28. The recorded curve may be well fitted by the Gaussian curve and allows us to state the standard deviation of Gaussian distribution σ [μm]. If we take into account also the photo-absorption coefficient μ [cm^2/g] for wavelength 13.4 nm (in Table 6) we can evaluate the gas mass density on the line as $\rho_0(\Delta z)$ [g/cm^3] for each studied gas.

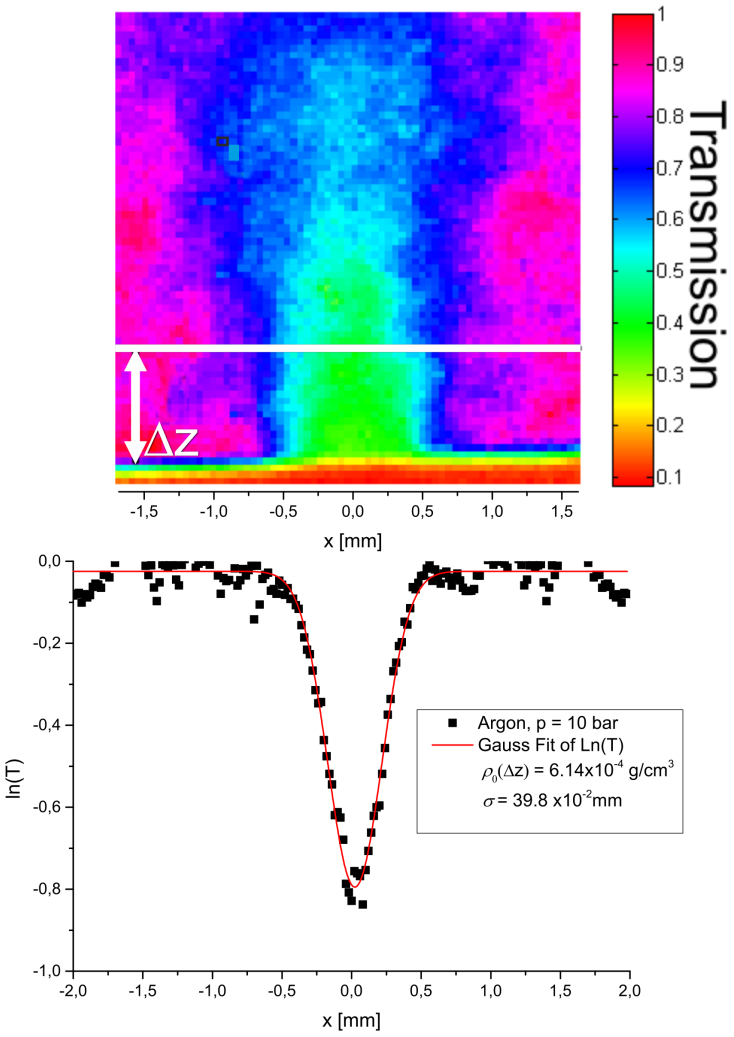

Fig. 28: *Up - Radiograph for Argon target; reservoir pressure p_{in} = 10 bar, exposure time delay Δt_R = 999 μs. Down - Logarithm of Argon gas-puff target transmittance at the distance Δz = 500 μm from the nozzle; the red line is the Gaussian fit. [57]*

Figure 29 shows the logarithm of transmission of Krypton (a) and Nitrogen (b) at the distance $\Delta z = 500$ μm and input pressure $p_{in} = 10$ bar.

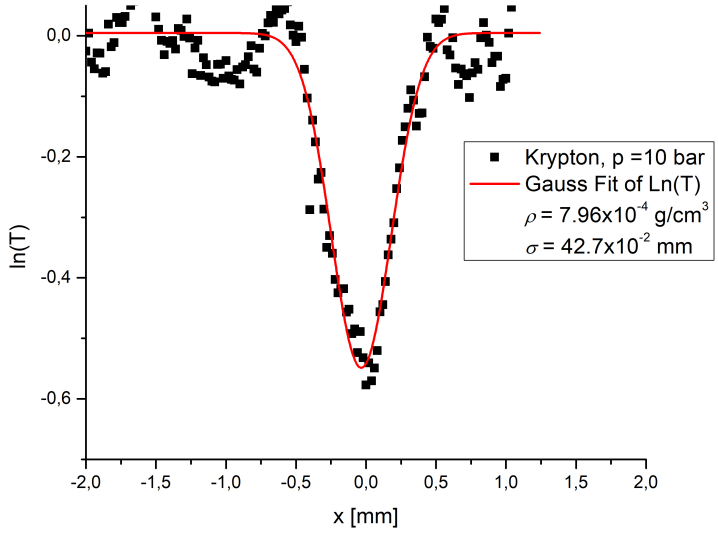

(a)

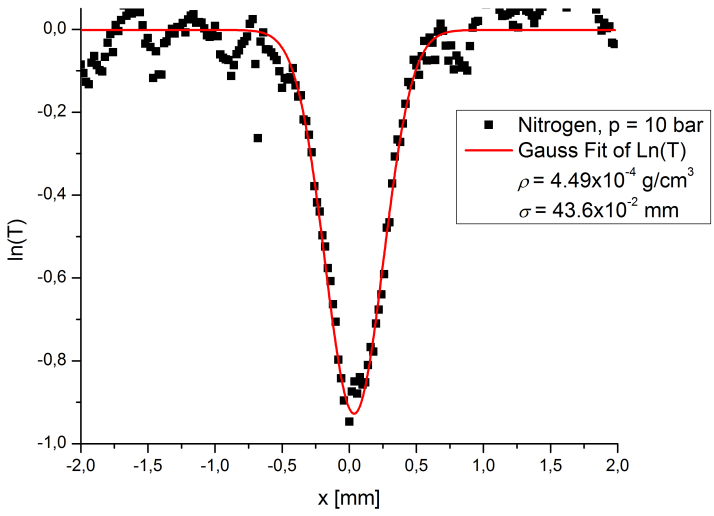

(b)

Fig. 29: *Logarithm of transmission of Krypton (a) and Nitrogen (b) at the distance* $\Delta z = 500$ μm *from the nozzle,* $p_{in} = 10$ *bar,* $\Delta t_R = 999$ μs.

The method can be used to determine experimentally the mass density space distribution of any gas emerging from the nozzle for different input pressure p_{in}. However, due to the limits of measuring equipment, we did radiographs for selected gasses at the intervals given in the Table 7. From these measurements, we determined the maximum resulting mass density at the distance $\Delta z = 500$ μm by the formula 4.7 and then we calculated the particle density N from equation 4.8. A comparison of basic gas-puff target parameters for the same pressure $p_{in} = 8$ bar is seen in Table 8. We depicted the particle densities N in the graph (Fig. 30) for better visualization.

Gas	**pressure p_{in} interval [bar]**
Argon	7 - 12
Krypton	8 - 15
Nitrogen	5 - 8

Table 7: *Overview of used input pressure p_{in} for Ar, Kr and N for estimation gas mass density.*

Gas	**Atomic number**	**Molecular weight**	**Particle density N [cm^{-3}]**	**Radial dimension σ [μm]**
Argon	18	39.948 u	5.4×10^{18}	392
Krypton	36	83.798 u	5.9×10^{18}	424
Nitrogen	7	28.013 u	5.3×10^{18}	431

Table 8: *Gas-puff target parameters. $p_{in} = 8$ bar*

The parameter of Gaussian function σ is very similar for all profiles. It shows that the width of gas-puff target depends mostly on the nozzle profile not on the gas type.

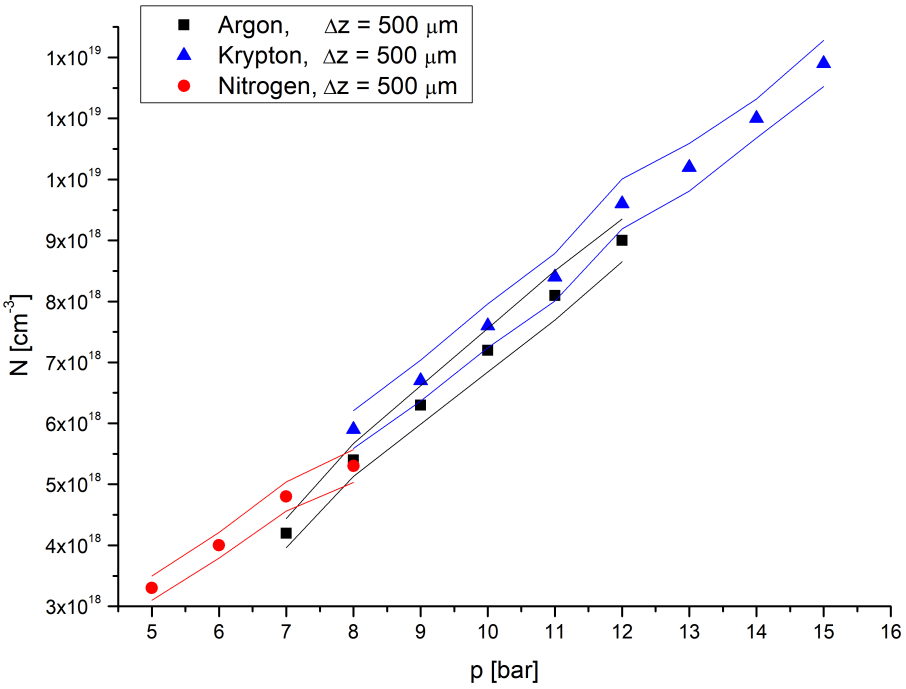

Fig. 30: *Comparison of particle densities N for Argon, Krypton, Nitrogen on selected input pressure intervals.*

Results for Used Nozzle

As we use the plasma source, the nozzle is ablated due to its proximity to the gas-puff target. From the measurement above we know that the shape of the gas stream is affected by the nozzle profile. After several plasma creations and laser shots the height decreases and spherical shape on the output is broken (Fig. 31). We investigated how the mass density and then particle density are changing after 2000 shots.

Fig. 31: *Detail of our single stream nozzle after 2000 shots.*

The radiograph and logarithm of transmission at the distance $\Delta z = 500$ μm for

used the nozzle are shown in Figure 32. On the shadowgraph, we can see the undulated surface. This damage is an occasion of lower gas density at the same distance as by new nozzle. To obtain higher mass density the focal point has to be moved closer to the nozzle. But this causes worst damage to the nozzle. The actual solution to this problem is to change the nozzle after a defined count of shots before the damage proves itself.

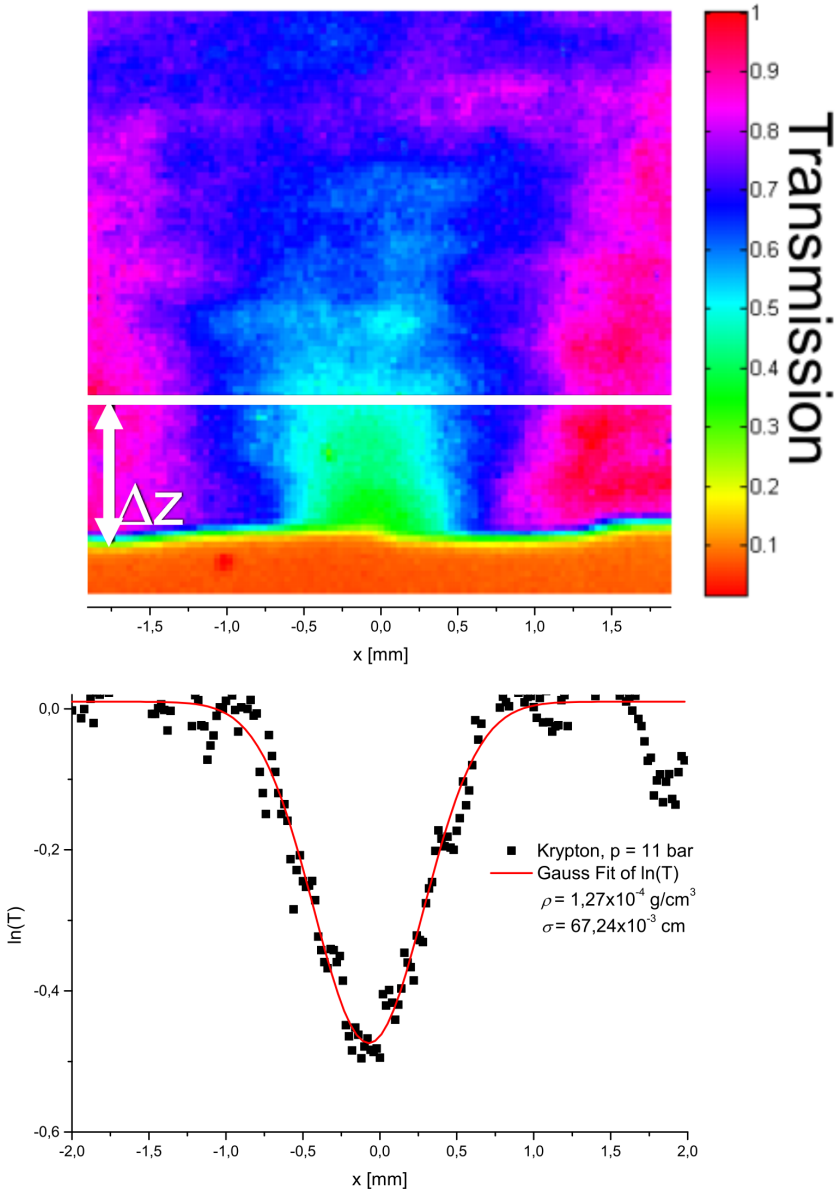

Fig. 32: *Up - Radiograph for Krypton target; reservoir pressure p_{in} = 11 bar, exposure time delay Δt_R = 999 μs. Down - Logarithm of Krypton gas-puff target transmittance at the distance Δz = 500 μm from the nozzle; the red line is the Gaussian fit. [57]*

In Figure 38 we show the comparison of particle density N for new and used single stream nozzle. The drop in density N is almost one order. This is due to a decrease of nozzle border. Parameter Δz is misleading in this case, because the jets starts to create itself below the edge of the nozzle.

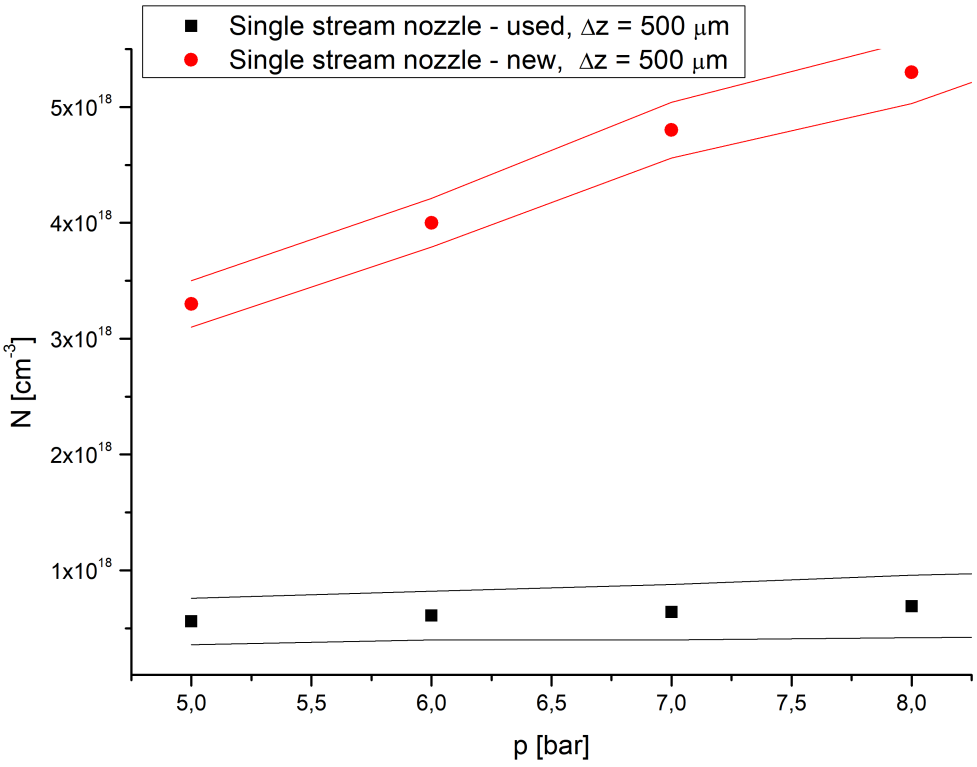

Fig. 33: *Comparison of particle density N according to input pressure for new and used single stream nozzle.*

Double Stream Nozzle

Another way how to increase the gas mass density is to use another type of nozzle with a different shape or based on different principle like double stream. Double stream nozzle [58] is used in laboratories in the Institute of Optoelectronics, Military University of Technology, Warsaw, Poland. This system uses 2 different gasses to create the gas-puff target and work under lower pressure up to 8 bars. The nozzle uses as working gas Nitrogen, Xenon and Krypton, and Helium as surrounding gas that helps to create a narrower and denser stream.

This system allows us to get the same particle density N as our SXR source system, but farther from the nozzle which means that the nozzle is not damaged and the gas-puff target is stable in time. This nozzle type has also its disadvantages that we will describe later.

The double stream nozzle particle density radiograph is shown in Figure 34. The distance Δz is 1 mm. The mass density depends on working and surrounding gas pressure, the delay between gasses injection and the time delay between opening nozzle and the laser pulses generation.

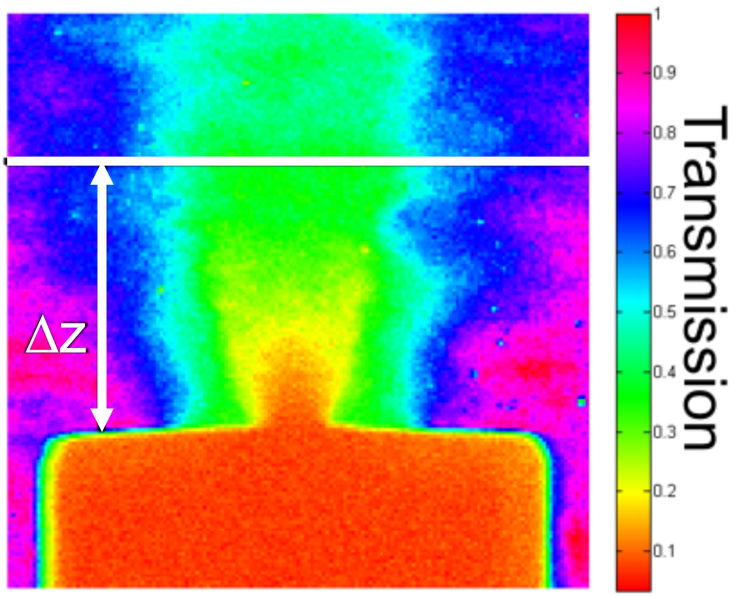

Fig. 34: *Radiograph for double stream nozzle using Krypton at pressure p = 12 bar, Δz = 1 mm and delay between gasses Δt_i = 750 μs.*

In principle, the whole system works on a very similar base like our SXR source

system. The main difference is that after opening the valve with working gas the surrounding gas starts to flow into the vacuum chamber and the surrounding gas narrows the working gas stream. Very important is the order of gasses and also the time delay between them.

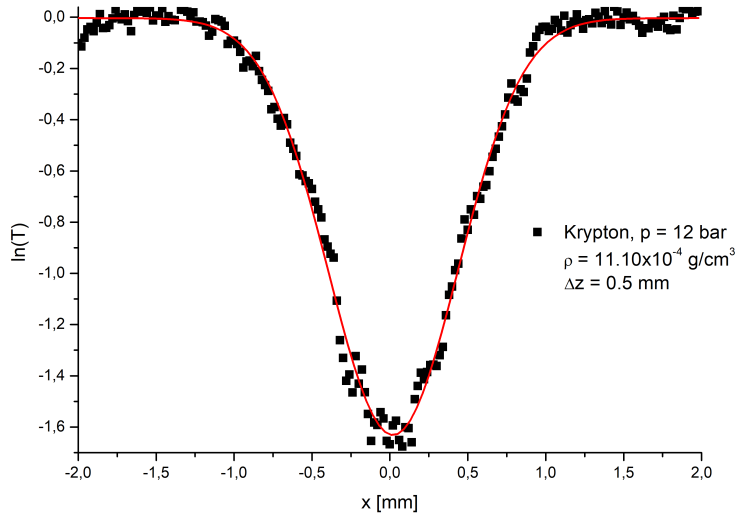

(a)

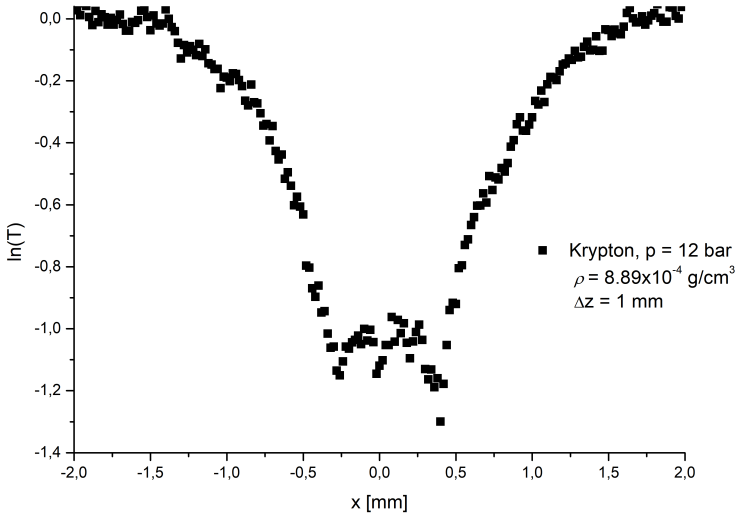

(b)

Fig. 35: *Krypton logarithm of transmission at pressure $p = 12$ bar, $\Delta t_i = 750$ μs and distance a) $\Delta z = 0.5$ mm from the nozzle, b) $\Delta z = 1$ mm from the nozzle.*

The logarithm of transmission for Krypton is shown in Figure 35 at the distance $\Delta z = 0.5$ mm and $\Delta z = 1$ mm. As is shown, at the distance $\Delta z = 0.5$ mm the profile can be fitted by Gaussian function. In the second case, the maximum is wider. However, this shape has not decreased the effect on plasma creation. Comparison of particle densities N in double stream nozzle for 2 different distances is shown in Figure 36.

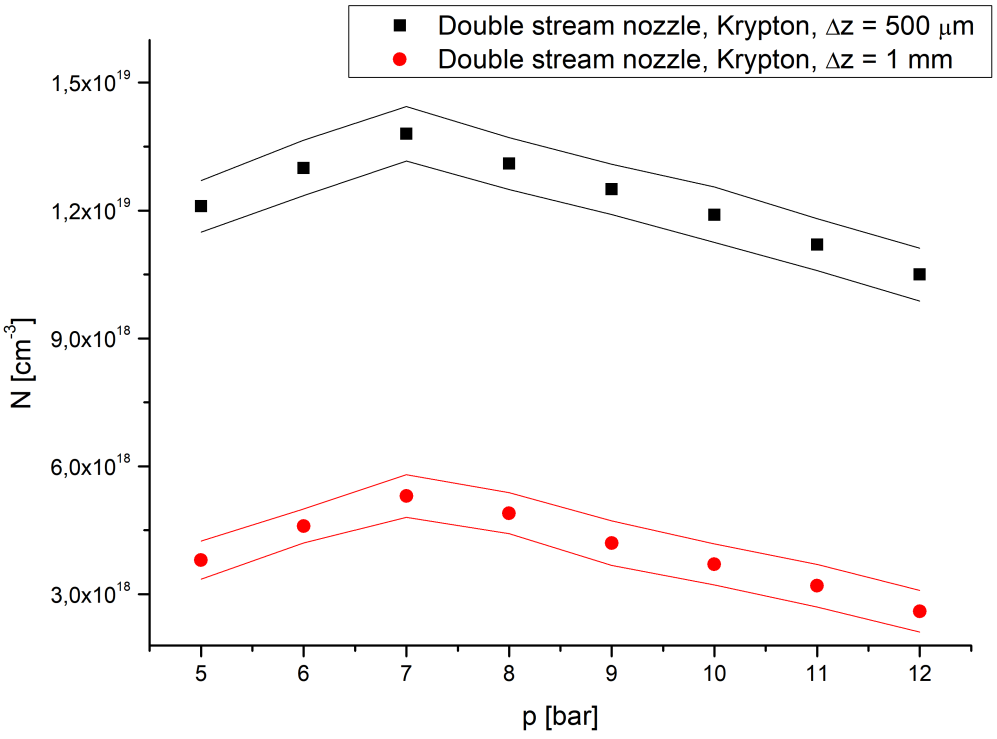

Fig. 36: *Krypton particle densities N versus input pressure p_{in} at $\Delta z = 500$ μm and $\Delta z = 1000$ μm for double stream nozzle.*

The double stream nozzle gas density depends also on time delay. The changes of mass densities ρ and particle densities N at the distance $\Delta z = 1$ mm for the different delay Δt_i between opening working gas (Xenon) and surrounding gas (Helium) are shown in Table 9. The radiograph for Xenon is shown in Figure 37.

ρ [g/cm^3]	N [cm^3]	Δt_1 [μs]	Δt_2 [μs]	Δt_3 [μs]	Δt_4 [μs]
1.12×10^{-3}	1.37×10^{18}	500	500	500	500
9.60×10^{-4}	1.17×10^{18}	500	500	400	600
9.42×10^{-4}	1.15×10^{18}	500	500	300	700
1.03×10^{-4}	1.26×10^{17}	500	500	300	700
1.03×10^{-3}	1.26×10^{18}	600	400	200	800
9.95×10^{-4}	1.22×10^{18}	650	350	200	800
7.05×10^{-4}	8.67×10^{17}	670	330	200	800
3.21×10^{-4}	3.93×10^{17}	700	300	200	800

Table 9: *Changes of mass densities ρ [g/cm^3] and particle densities N [cm^3] at the distance $\Delta z = 1$ mm for working gas Xenon and surrounding gas Helium for various time delay t_i. The time delay is indicated by the synchronization pulse: t_1 - valve opening for working gas; t_2 - injection of working gas; t_3 - valve opening for surrounding gas; t_4 - injection of surrounding gas*

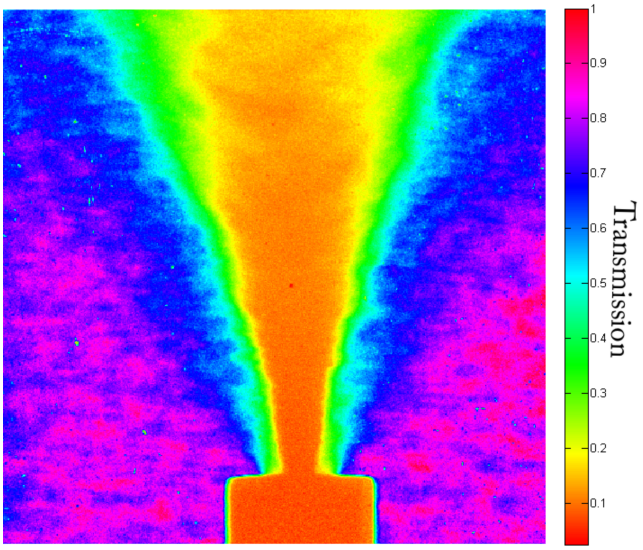

Fig. 37: *Radiograph for double stream nozzle using Xenon, $p = 8$ bar, $\Delta t_1 = 0.67$ ms, $\Delta t_2 = 0.33$ ms, $\Delta t_3 = 0.20$ ms, $\Delta t_4 = 0.80$ ms.*

Comparison of Single and Double Stream Nozzles

The comparison between single and double stream nozzles:

- double stream nozzle operates with similar particle density like single stream nozzle under lower pressure (Fig. 38);
- double stream nozzle optimization function depends also on surrounding gas input pressure and working and surrounding gas valve sync-time as well;
- focal plane for double stream nozzle is farther from the nozzle that does not leads to nozzle damage;
- for the single stream nozzle we set only one time delay Δt according to four Δt_i in double stream nozzle.

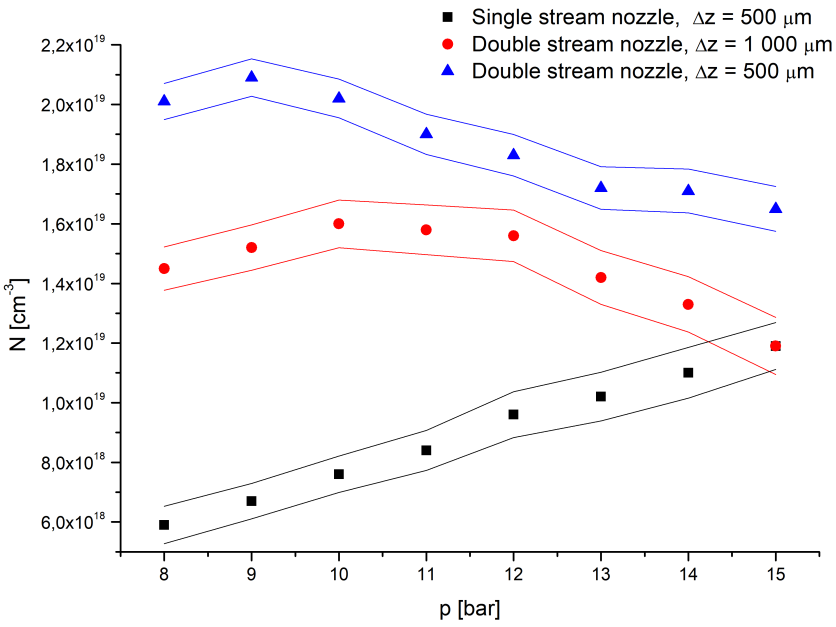

Fig. 38: *Comparison of particle densities N for single and double stream nozzle according to input pressure.*

4.2 Computer Modelling

4.2.1 Simulations of Mass Density in Gas-puff Target

In this part, we focus on computer modelling of the dynamically opened nozzle. This is very useful to predict experimental results or find new possibilities on how to optimize the SXR source. For simulation, we used 2 different programs. First is 2D RMHD (Radiation-Magneto-Hydro-Dynamic) code Z* (EPPRA s.a.s., France) [59]. Second, for verifying results, we used code ANSYS [61]. The Z* code offers also the possibility to simulate the plasma radiation and is very useful as a complex program for optimization of the SXR source system.

Z* Code

The Z* (or Zstar) code is numerical modelling tool developed for complete simulations of the behavior of a multicharged ion plasma in experimental and industrial facilities, using RMHD formalism. It is derived from the well-proven code Zeta [60], developed for the purposes of plasma modelling in HEDP by the same team that put together Z*.

The Zstar code is designed in a 2D axially symmetric geometry with full radiation transport. Interpolations of preliminary prepared databases allow the code to avoid online calculations of variety of processes such as plasma dynamics, atomic physics, and ion kinetics. The Z* also includes an interactive interface for graphical adaptive computation-grid construction. [59]

The Zstar code works with grid that corresponds with real proportion of the nozzle. This code has its limits in dimensions of the model and we have to take in count the grid borders that can be counted as solid obstacle for the gas stream in some cases. We will talk about this problem later.

Input Parameters

The Zstar code uses 3 main files that the user have to fill and several predefined data files that are selected based on the assignment.

a) Data Initial FLUX dt - text file

b) Data Laser - text file

c) Grid - graphically file

a) Data Initial FLUX dt

This text file contains 21 input parameters that are shown in Table 11. This file serves all tasks, such as simulating gas flow, emitting plasma from a gaseous target, or simulating capillary discharge. As a result, some parameters remain zero for different tasks.

b) Data Laser

For the simulation of laser-produced plasma, we have to enter the laser data for this file. It contains 10 parameters that are in Table 10. In the case of gas-puff target simulation, we do not use this file, but we will list it here because in the chapter 5.1 we will refer to it.

Input parameter	**Unit**
focal length	mm
beam diameter	mm
focus position by Z	mm
focal spot diameter	mm
pulse (gaussian) FWHM	ns
wave-length	nm
laser energy	J
pulse time delay	ns
Read laser-power data from file	-
Data file name	-

Table 10: *Input parameters for Zstar code in "Data Laser".*

c) Grid

The grid serves as counting mesh and also as the graphical expression of the task. It has cylindrical symmetry around the chosen axis. Each crossing corresponds to the counting point with boundary conditions from surrounding points. It leads to mesh refinement in parts where there are significant changes. The grid boundaries also correspond with real boundaries which means that the models have to be big enough or the influence of boundaries have to be minimal. The grid is created in program ZAGCII, developed also from EPPRA.

Input parameter	Explanation
c1	Amount of radiation groups; Angle groups
c2	Start TIME [μs] - Time of start the computation. It can not correspond with start of the process.
c3	Expected time scale of current pulse in μs
c3-1	Maximal time-step (μs) (by default c3/10000)
c4	Geometry proportion by R, Z
c5	Minimum density (vacuum) (g/cm^3)
c6	Time interval for output data (ns)
c7	Special radiation group number
c8	Initial "effective pre-ionization degree" in plasma channel
c9	Quantity of substances in the task (should co-inside with total number in c16)
c10	Quantity of substances in electrodes
c11	Graphical markers of substances in electrodes (amount should co-inside with c10)
c12	Quantity of substances in insulators
c13	Graphical markers of substances in insulators (amount should co-inside with c12)
c14	Substance number of gas (plasma)
c15	Quantity of graphical markers including 0
c16	Correspondence between graphical markers, substance numbers and density (marker; number; density)
c17	Initial gas or plasma temperature in eV
c18	Initial electron temperature in pre-ionized channel (eV)
c19	Gas (plasma) coef. adiabatic (must be >1)
c18	Gas (plasma) flux (scm^3); pressure in feeder (Torr); pressure in chamber (Torr)
c19	Capillary position if exist from (cm) to (cm)
c20	To read density distribution data from file put 1 otherwise put 0
c21	If data read from file (previous key=1) put full file name otherwise DensityDistribution.plt

Table 11: *Input parameters for Zstar code in "Data Initial FLUX.dt" with their explanation.*

Model of Single Stream Nozzle

Our first task was to verify simulated data because the Z* was never used before for gas expansion. We prepared the models of single stream nozzle used is our SXR source system in ZAGCII (for Z*) and in Ansys and compared the computed data. The nozzle cross-section is shown in Figure 21. Nozzle height is 1 mm and the output diameter is $d = 0.54$ mm.

The Ansys is a well-known and frequently used program, unlike The Zstar, and we do not mention step-by-step modeling, but only present the data obtained.

For Zstar we made a grid (Fig. 39) with the cylindrical symmetry around the nozzle axis. The model of the vacuum chamber and the reservoir of the input gas was done in ZAGCII. The grid corresponds to half of the nozzle along the symmetric axis (see in detail in Fig. 39). As working gas, we used primarily Nitrogen because of the most common use. After verification, we also simulated the flow of Argon and Krypton in Zstar.

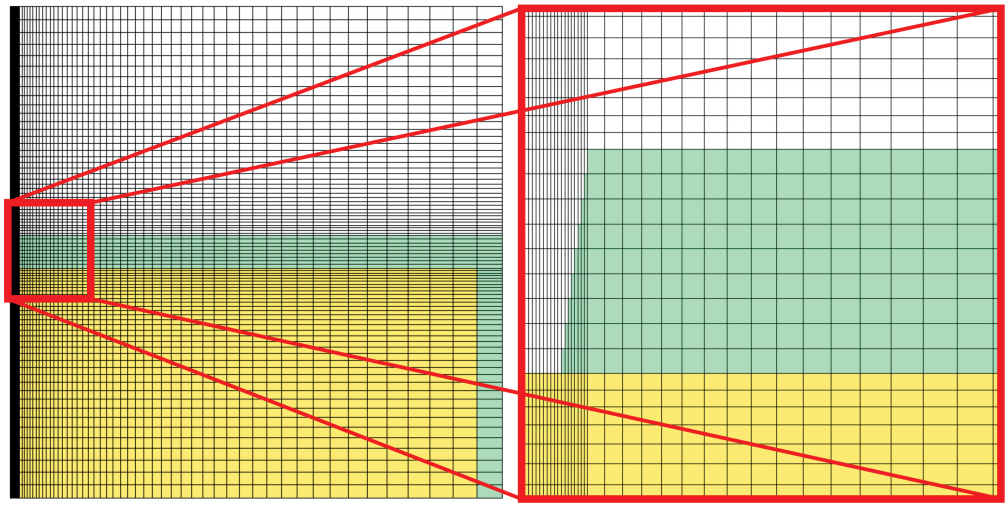

Fig. 39: *Grid of the nozzle with gas reservoir and vacuum chamber. Green – metal nozzle, yellow – gas reservoir, white – vacuum chamber; proportions: 15×15 mm.*

The most important parameters from *Data Initial FLUX dt* for our model are shown in Table 12. We present input data for the Nitrogen model. The input pressure p_{in} is gas pressure before entering the valve. Typically, this pressure is in the range from 5 to 20 bars. p_b is background pressure in the vacuum chamber.

Nitrogen input pressure	$p_{in} = 10$ bar
Background pressure	$p_b = 10^{-7}$ bar
Nitrogen mass density at p_{in}	$\rho_{in} = 1.129 \times 10^{-2}$ g/cm^3
Background mass density at p_b	$\rho_b = 1.100 \times 10^{-10}$ g/cm^3
Nozzle density	ρ_n =7.86 g/cm^3
Proportions	15 × 15 cm

Table 12: *Input parameters for gas expansion from single stream nozzle into ultra high vacuum.*

In Figure 40 we can see the comparison of Nitrogen mass density counted via Zstar and Ansys. Input pressure in $p_{in} = 10$ bar and the mass density was taken at distance $\Delta z = 0.5$ mm after 1 ms expansion into the vacuum chamber. The shapes and maximum mass density are very similar. It means that we can use Zstar for simulation gas flow and the next simulations are done via Z*.

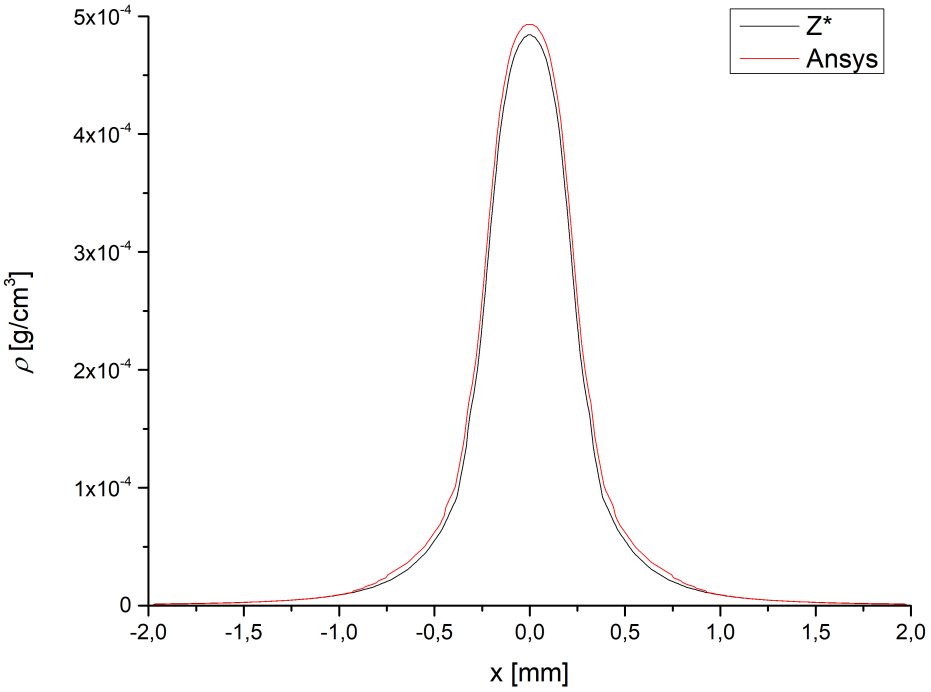

Fig. 40: *Comparison of Nitrogen mass density at the distance $\Delta z = 0.5$ mm for input pressure $p_{in} = 10$ bar in time $\Delta t_E = 1$ ms calculated via Zstar and Ansys.*

Working Gas Expansion into Ultra High Vacuum

We simulated gas expansion from single stream nozzle into ultra high vacuum that corresponds with our SXR source. The evaluated spatial distribution of Nitrogen mass density is seen in Fig. 41. The input pressure is $p_{in} = 10$ bar, background pressure $p_b = 10^{-7}$ bar and time of expansion $\Delta t_E = 1$ ms. Coordinate R corresponds with coordinate x in radiography measurements.

We are interested in mass density at distance $\Delta z = 0.5$ mm from the nozzle where the laser beam is focused. Computed profile of mass density ρ along the transversal coordinate x via Z* is shown in Figure 42.

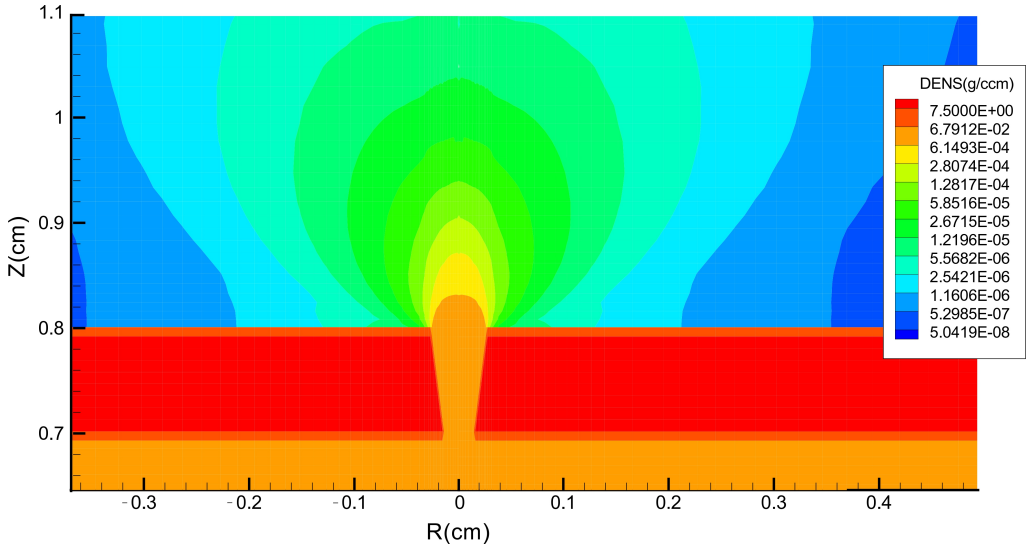

Fig. 41: *R-Z dependence of Nitrogen expansion from single stream nozzle into ultra high vacuum.*

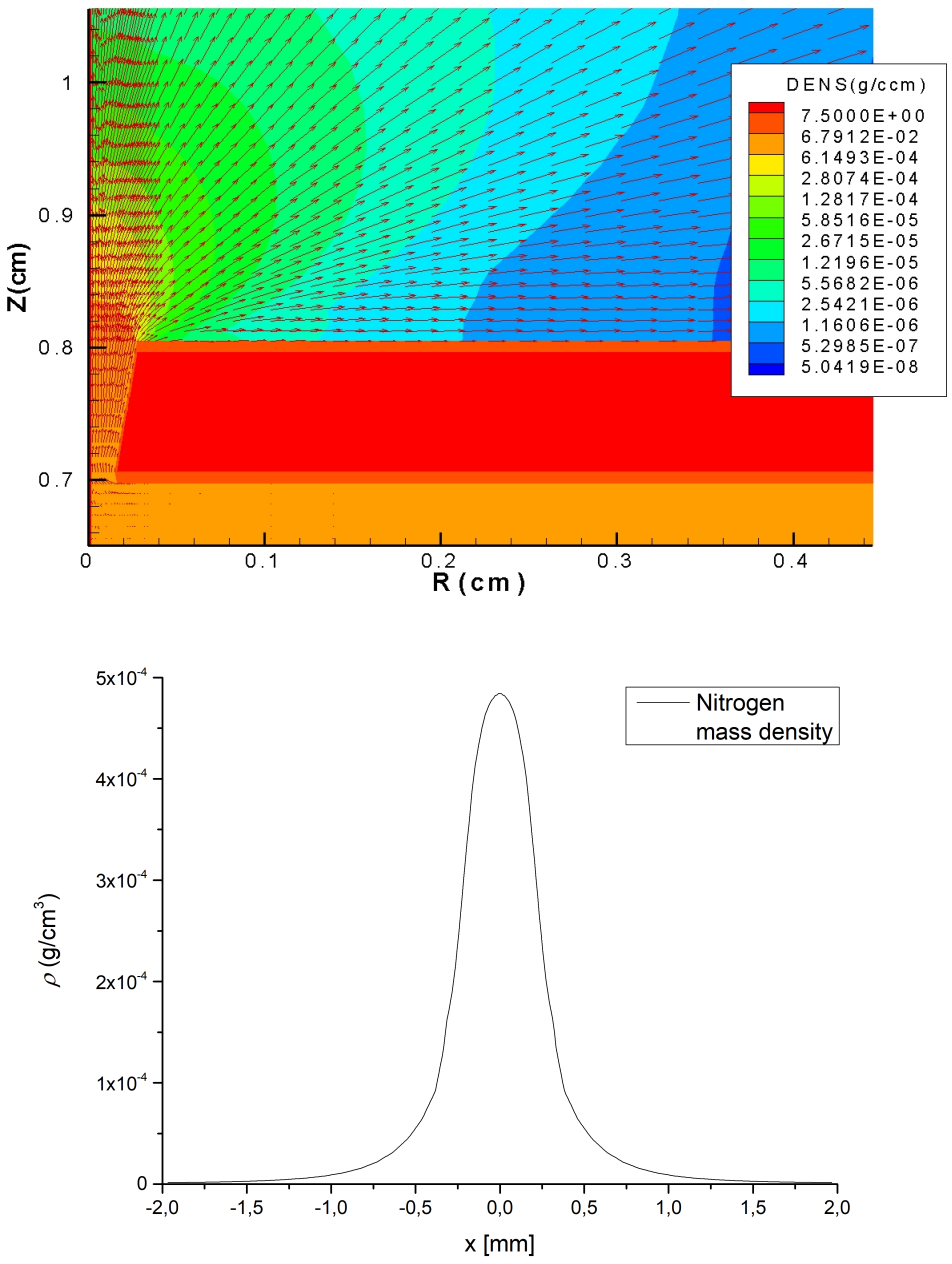

Fig. 42: *Detail of Nitrogen expansion with velocity vectors and profile of Nitrogen mass density at distance* $\Delta z = 0.5$ *mm. Input pressure is* $p_{in} = 10$ *bar, background pressure* $p_b = 10^{-7}$ *bar and time of expansion* $\Delta t_E = 1$ *ms.*

As we know from chapter 3 the output radiation depends also on time delay Δt between valve opening and laser action. In Manual was recommended $\Delta t = <900;1400> \mu$s, we estimated the best range for our SXR source system is $\Delta t = <1050;1200> \mu$s. We are interested in stability of the mass density in gas-puff target. We choose 3 time delay and compared the Nitrogen mass density at the same distance $\Delta z = 0.5$ mm. Result is shown in Figure 43. We can see that the mass density ρ is stable and have no effect on gas-puff target. This is important for optimization function $F(E_{out})$. The output radiation depends on both parameters but the parameters are each other independent and we can fix ρ when we determine Δt.

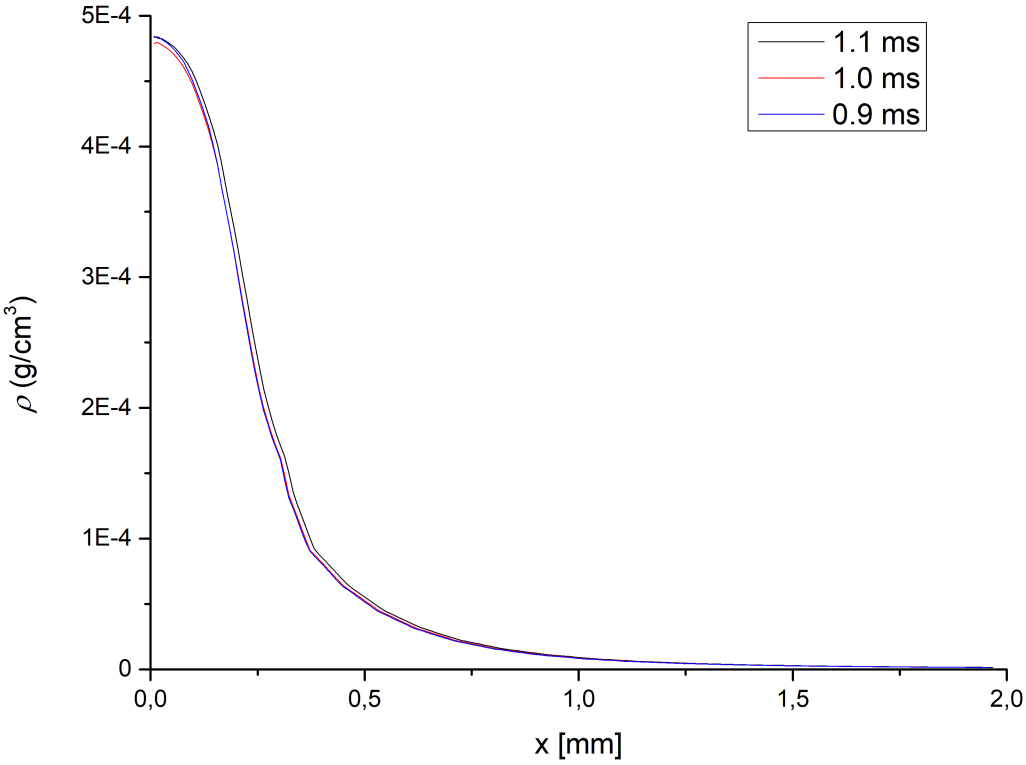

Fig. 43: *R-Z dependence of Nitrogen expansion from single stream nozzle into ultra high vacuum.*

Our goal was to compare computed and experimental data which is seen in Figure 44. We can see that both curves have similar shapes and values ρ are very close. That knowledge gives us the opportunity to design new setup of SXR source system before its real implementation. The simulated data give us real idea of of the expected outcome.

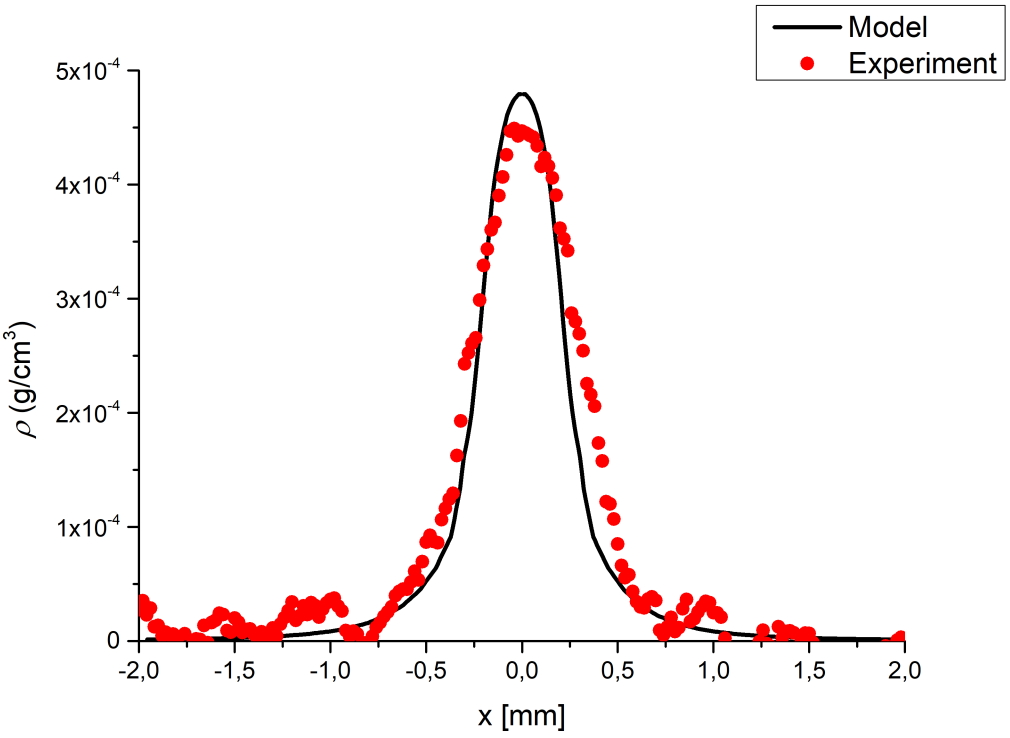

Fig. 44: *Comparison of the experimental and computed data of Nitrogen mass density ρ at distance $\Delta z = 0.5$ mm, input pressure $p_{in} = 10$ bar, $\Delta t_E = 1$ ms.*

We calculated also data for Argon and Krypton and results for all 3 gasses are in Figure 45. From simulations, we obtained the particle density N in the range from 5 to 20 bars for all 3 gasses that can be used in our SXR source system. Figure 46 shows us that with higher pressure the particle density increases. Due to the fact that for higher N we get more photos/sterad, we can change the piezoelectric valve and operate the SXR source system on higher pressure.

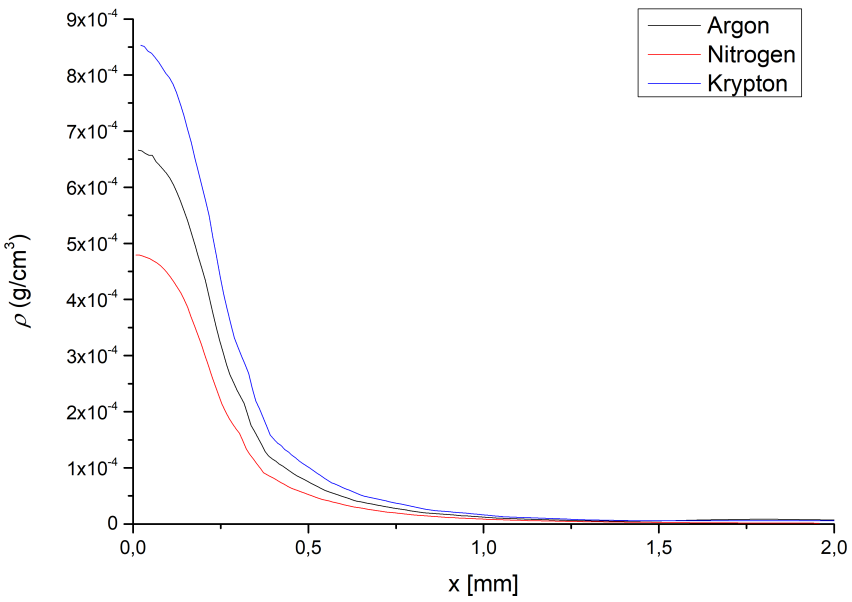

Fig. 45: *Argon, Krypton and Nitrogen mass density ρ at distance $\Delta z = 0.5$ mm, input pressure $p_{in} = 10$ bar, $\Delta t_E = 1$ ms.*

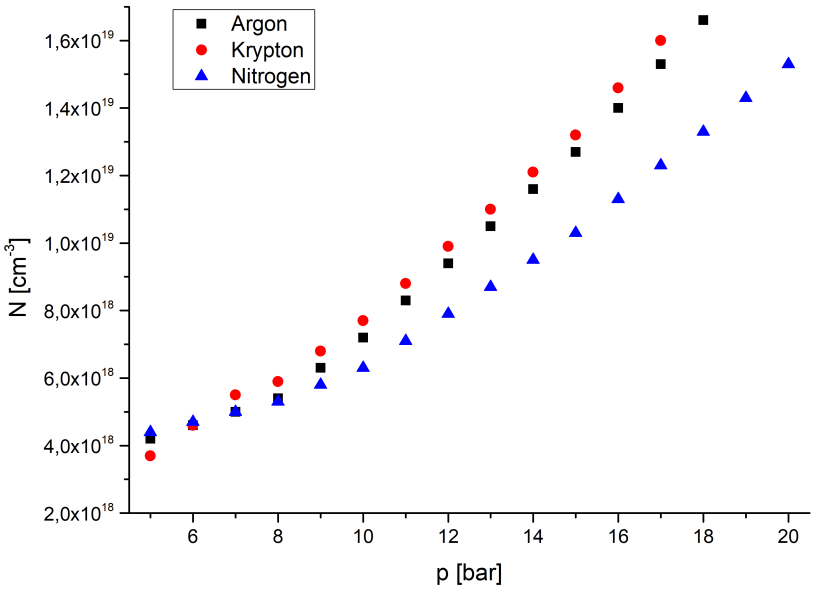

Fig. 46: *Simulations of Argon, Krypton and Nitrogen particle density N for various pressures.*

4.2.2 Working Gas Expansion into Chamber Filled by Background Gas

One of the big disadvantages of our SXR source is nozzle ablating. We presented in chapter 4.1.1 how the mass density decrease in time due to nozzle changes. This problem can solve the double stream nozzle but it becomes more complicated to set up the system than the single stream nozzle. We tried to find another way how to shift the gas-puff target while maintaining the same density.

Possibilities of how to change the distance Δz but preserve the mass density is to make barrel shocks with Mach disk [62]. Measurement of such Mach disk with a similar nozzle as ours was published by Tobias Mey. The main idea was to increase background pressure [63].

In the expanding flow the Mach number M is connected with the cross sectional area A of the flow by the well-known area relation of gas dynamics:

$$\frac{A}{A_*} = \frac{1}{M}\left[\frac{2}{\gamma+1}\left(1+\frac{\gamma-1}{2}M^2\right)\right]^{\frac{\gamma+1}{2(\gamma-1)}} \tag{4.9}$$

where γ is the ratio of the specific heats and A_* the throat area. For diatomic gases ($\gamma = 7/5$), the Mach number at the nozzle exit is equal to $M_e \approx 2.6$. The structure of the shock system depends on the nozzle pressure ratio. For sonic nozzles and pressure ratios $15 < p_{in}/p_b < 17\,000$, the distance y_M between the nozzle exit and the Mach disc is given by the correlation $y_M/d_e = 0.67\ (p_{in}/p_b)^{1/2}$ [64].

In the isentropic flow within the barrel shock, the density ρ is a function only of the Mach number and the input density ρ_{in}:

$$\rho = \rho_{in}\left(1+\frac{\gamma-1}{2}M^2\right)^{-\frac{1}{\gamma-1}} \tag{4.10}$$

We prepared the model for simulation Mach disk. As background gas we used Helium with $\rho = 8.835{\times}10^{-5}$ g/cm^3 at $p_b = 5 \times 10^{-2}$ bar. Working gas was Nitrogen at $p_{in} = 10$ bar because it is commonly used gas in our laboratory. Expansion into vacuum is shown in Figure 47.

If we compare the profiles of Nitrogen density in ultra high vacuum and in high vacuum (case with Helium as background pressure), we can see that Helium help to straighten the gas stream. Mass density for expansion into ultra high vacuum at the distance $\Delta z = 0.5$ mm is $\rho = 4.84{\times}10^{-4}$ g/cm^3. If the Nitrogen expands into the

Helium the mass density is $\rho = 5.12{\times}10^{-4}$ g/cm^3 at distance $\Delta z = 1$ mm (Fig. 48). It means that we can shift the gas-puff target farther from the nozzle.

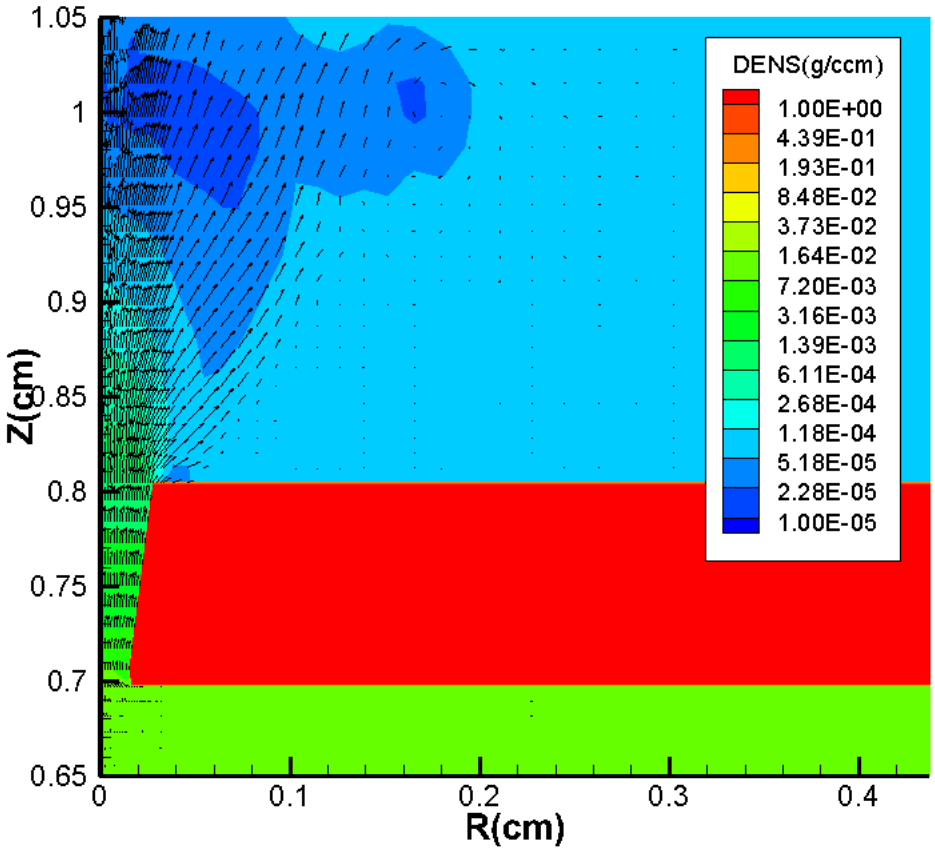

Fig. 47: *Nitrogen expansion into vacuum chamber with background pressure $p_b = 5{\times}10^{-2}$ bar for input pressure $p = 10$ bar.*

From these results, it seems to be better to use the SXR source system only with a high vacuum. But in this case attenuation of SXR radiation in the vacuum chamber is increasing. Possibility of solving this problem is to use two vacuum chambers and differential pumping.

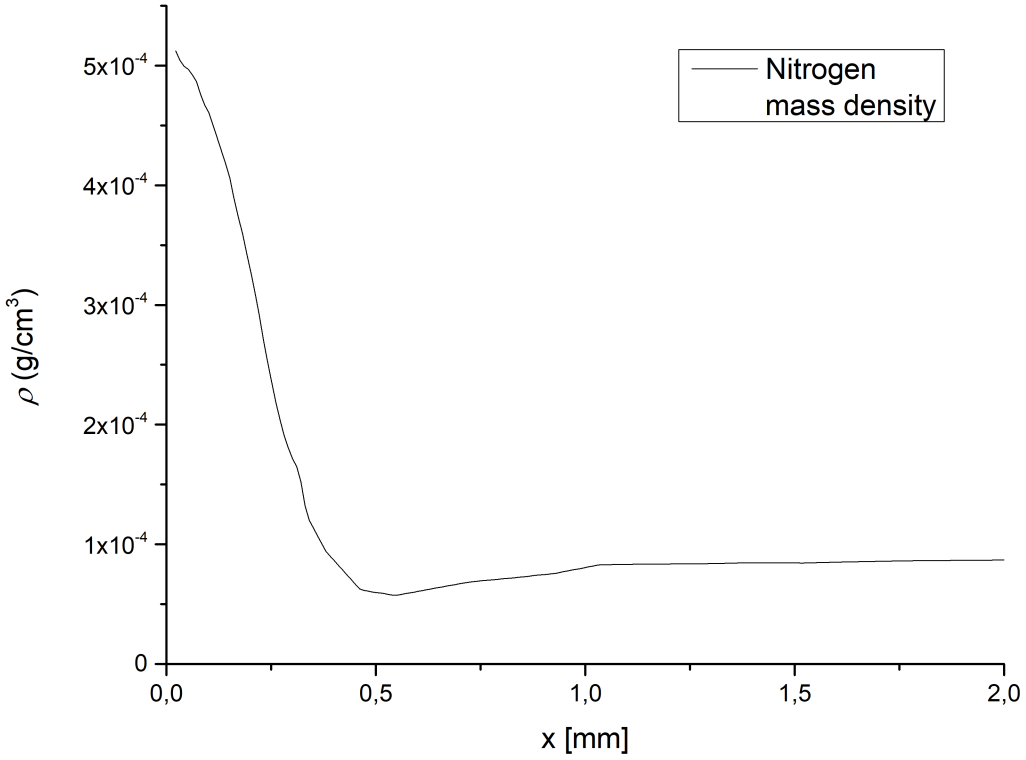

Fig. 48: *Nitrogen mass density at distance Δz = 1 mm for expansion into vacuum chamber with background pressure $p_b = 5{\times}10^{-2}$ bar.*

4.3 Summary for Optimization Function $F(E_{out})$

We studied the parameters of optimization function $F(E_{out}) = F(\lambda, E_{in}, f, \Delta t, h, \rho, \Delta z, p_{in}, p_b)$ to improve the SXR source system. We tried to preserve the user friendly set up with as little element as possible and high photon flux. If we find parameter dependency and define parameter reciprocally on the whole system we can prepare the set up of similar systems for future use in other laboratories.

The studied parameters can be divided into 3 categories:

Parameters with minimal effect on the optimization function

- Excitation laser wavelength λ
- Laser repetitive frequency f
- Depth of field of Nd:YAG laser in the focal plane h

Parameters that increase the photon flux but are limited by our system

- Excitation laser energy E_{in}
- Input gas pressure p_{in}

Parameters with effect on other parameters

- Time delay between valve opening and excitation laser pulse Δt
- Gas density in gas-puff target ρ
- Distance of the focal point from the nozzle Δz
- Background pressure in vacuum chamber p_b

In the first group are λ, f, h. Parameter λ is given by laser type, frequency and depth of field have very low effect on resultant photon flux and we can declare them by constants for each system. This leads to simplification $F(E_{out}) = F(E_{in}, \Delta t, \rho, \Delta z, p_{in}, p_b)$.

The second group is made up of parameters that are limited by the system. There is space for technical changes to our system and thus increasing photon flux. As was shown from simulations (Fig. 46) for higher input pressure p_{in} we get higher particle density N and then higher photon flux. In our system, we are limited by valve to pressure $p = 15$ bar.

An analogous case is for excitation laser energy E_{in}. We showed in Figures 14 and 15 that for higher excitation charging we get higher E_{in} and shorter laser pulse. If we use the marginal adjustment with excitation charging $U = 650$ V we get $E_{in} = 669$ mJ and $t = 6.8$ ns.

From these results, we can recommend the improvements of the SXR source system. In our case we can adjust these 2 parameters to the best settings. We can declare them constant for our optimization function.

The third parameter group is a set of parameters that are strongly dependent on each other or influence the other parameters. As was shown above, ρ and Δz are directly related and depend on input pressure. The distance has also effect on the nozzle ablating and subsequent change of the gas-puff target. Δt is one of the most sensitive parameters. The results depend on p_{in} and Δz which proves to be problematic when ablating the nozzle and subsequently changing the distance of gas-puff target. For each set of adjustments, the time delay has to be tune separately. The last parameter is background pressure p_b that can rapidly change the adjustment. On the other hand, if we change the background pressure all values change but the dependencies of individuals parameters stay the same and we can set it finally as constant for the whole SXR source.

All these results lead to simplifying the optimization function to form:

$$F(E_{out}) = F(\rho, \Delta z, \Delta t),$$

with static parameters λ, E_{in}, f, p_{in} and p_b.

We operate our SXR source system with following parameters:

- excitation laser wavelength $\lambda = 1\ 064$ nm,
- excitation laser energy $E_{in} = 669$ mJ ($U = 650$ V, $t = 6.8$ ns),
- laser repetitive frequency $f = 2$ Hz,
- input gas pressure $p_{in} = 15$ bar,
- background pressure in vacuum chamber $p_b = 10^{-7}$ bar.

5 Computer Modelling of SXR Emission from LLG source

5.1 Simulations of Plasma Radiation

Besides, plasma radiation and the number of photons/srad are given by parameters of the gas-puff target like shape and mass density ρ. In chapter above we investigated the mass density, its dependence on working gas and on input pressure and we computed the gas-puff target. In this part, we focused on simulations of plasma radiation based on experimental and calculated data of mass density ρ.

For simulations, we used output file of calculated mass density and also prepared grid (Fig. 49) with Gaussian profile that corresponds with measured data. For each gas and input pressure, we fit the measured data on this grid. The grid could be monochromatic with the highest value ρ_0, but in that case, the output radiation does not correspond properly with measured data and the model gives incorrect results. We recommend to use the input file or fit the input data according to obtained data from the previous investigation. In Table 13 the input laser data are listed. The laser data stay the same for all calculations with changing gas-puff target.

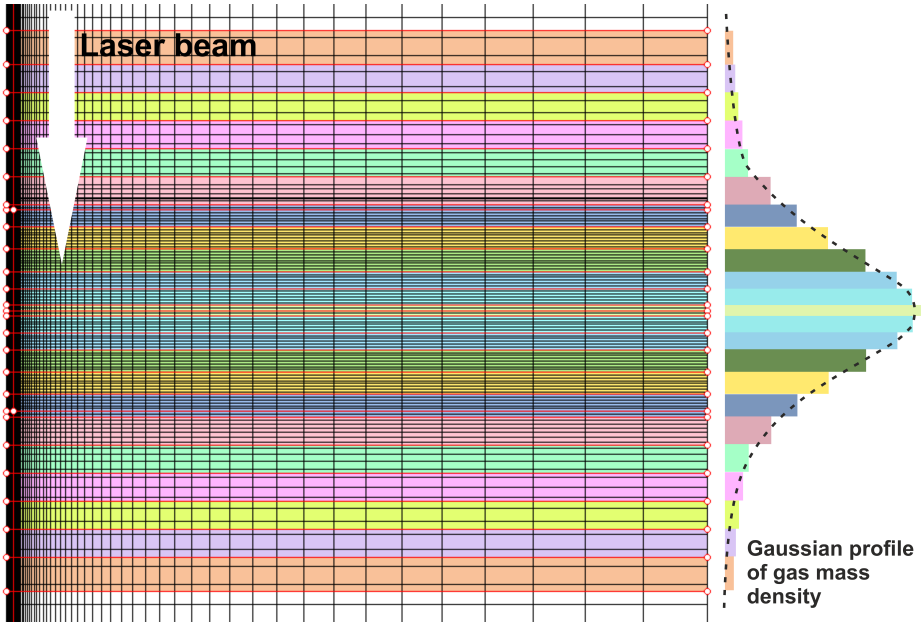

Fig. 49: *Grid of gas-puff target with Gaussian profile. Nitrogen, σ = 430 μm.*

Input parameter	Value
focal length	100 mm
beam diameter	6 mm
focus position by Z	2.5 mm
focal spot diameter	0.05 mm
pulse (gaussian) FWHM	7.7 ns
wave-length	1064 nm
laser energy	580 mJ

Table 13: *Input parameters for Zstar code in "Data Laser".*

We simulated the plasma radiation in the Nitrogen gas-puff target and compare the result with spatial distribution recorded by a pinhole camera. Input values for Nitrogen as working gas were $p_{in} = 10$ bar (e.g. $\rho_0 = 4.48 \times 10^{-4}$ g/cm^3), $E_{in} = 669$ nm, $t = 6.8$ ns. The comparison is in Figure 50.

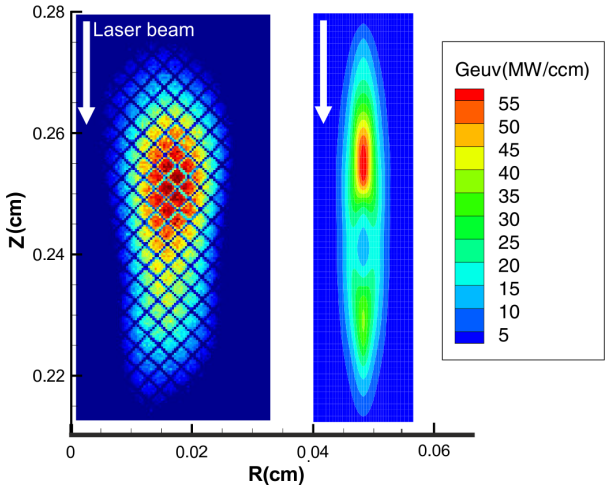

Fig. 50: *Comparison of Nitrogen plasma taken by pinhole camera and calculated distribution of emitted instantaneous power Q_{euv} from unit volume of plasma in the wavelength range 2.8766 - 2.8867 nm at time t = 10 ns. [54]*

Nitrogen plasma was imaged by a pinhole camera using the hybrid semiconductor pixel detector Timepix operated in the /Time-over-Threshold/ mode. The magnification of the camera was 16× while the source - detector distance was 344 mm. The pinhole diameter was 50 μm. A titanium foil filter of 0.4 μm thickness was used to obtain quasi-monochromatic radiation at ∼2.88 nm. The image is an average of 100 consecutive single-shot images recorded at 1 Hz repetition rate.

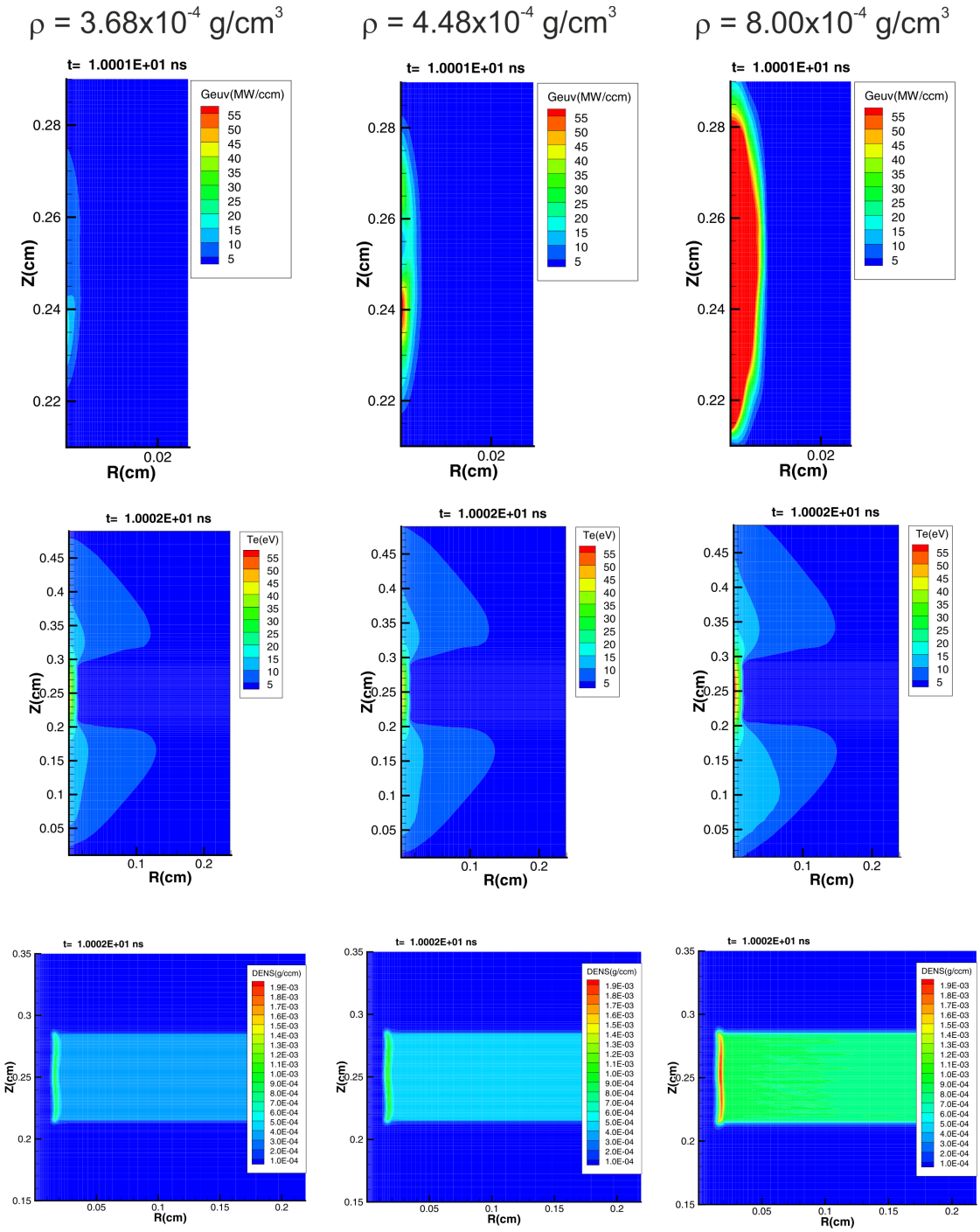

Fig. 51: *Distribution of emitted instantaneous power Q_{euv} from unit volume of plasma, plasma electron temperature T_e and plasma mass density in the wavelength range 2.8766 - 2.8867 nm at time $t = 10$ ns.*

The simulation were done primarily for Argon and Nitrogen that are used in our SXR source system. We got complete idea of plasma radiation and predicted values of irradiated photons/srad. In Figure 51 is comparison of plasma mass density, electron temperature T_e and distribution of emitted instantaneous power Q_{euv} from unit volume of plasma in the wavelength range 2.8766 - 2.8867 nm at time $t = 10$ ns for three different input Nitrogen mass density. As we can see if we increase twice mass density (third column) the output Q_{euv} rapidly increase. For better view we change range and result depicted in Figure 52. For all depicted distribution of emitted instantaneous power Q_{euv} we constructed graphs with horizontal (Fig. 53) and vertical (Fig. 54) profiles. The simulated radiation is shown in Figure 55.

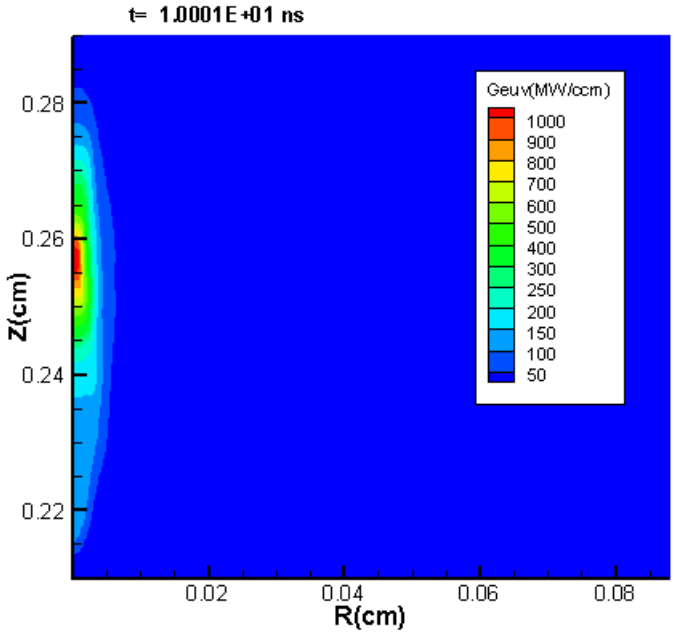

Fig. 52: *Distribution of emitted instantaneous power Q_{euv} from unit volume of plasma for Nitrogen mass density $\rho = 8{\times}10^{-4}$ g/cm^3.*

As as mentioned above, the model coincides with the retrieved data. From these results we can predict the SXR source system behavior and we have verified the proposed improvements.

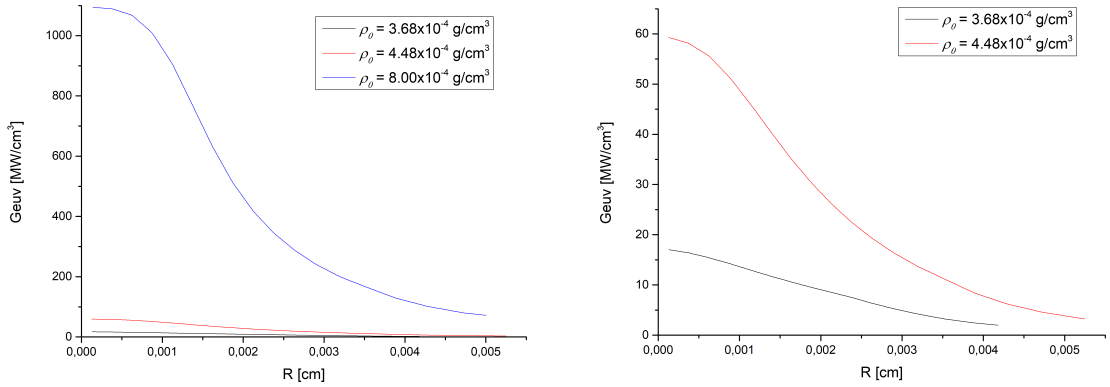

Fig. 53: *Horizontal profile of Q_{euv} for three input Nitrogen mass density and detail.*

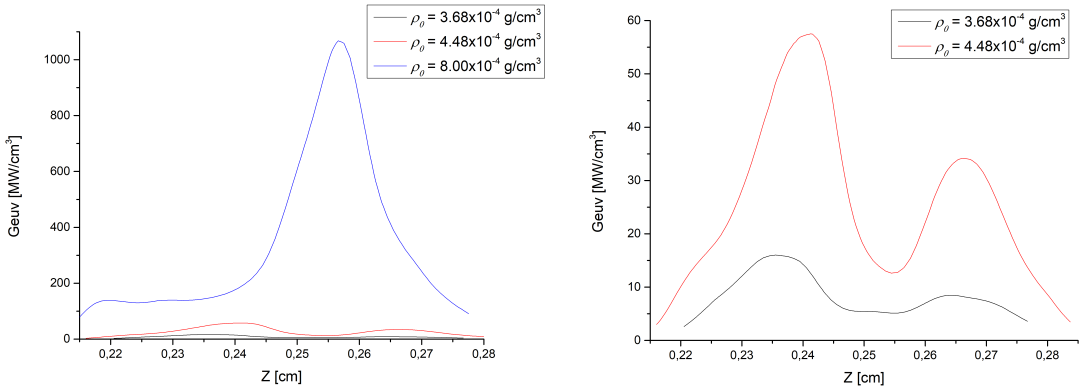

Fig. 54: *Vertical profile of Q_{euv} for three input Nitrogen mass density and detail of lower .*

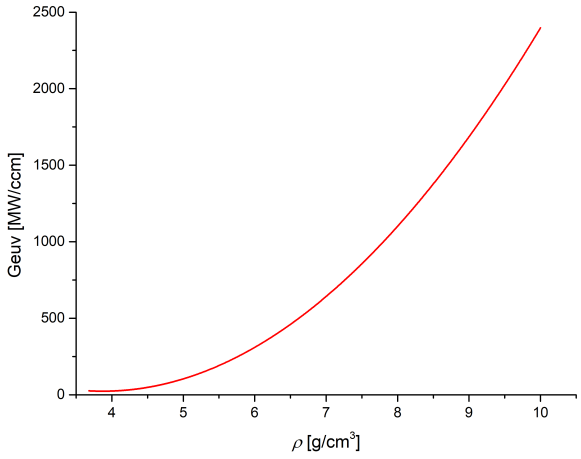

Fig. 55: *Calculated Q_{euv} dependence on mass density ρ.*

6 Biological Cell Imaging - Preliminary Experiment

6.1 Sample for our SXR Microcopy

We prepared the dehydrated sample of CT 26 fibroblasts, derived from colon carcinoma Mus musculus (strain BALB/c) for SXR microscopy. The specimens were prepared on 100 nm thick 1×1 mm Si_3N_4 membrane in 5×5 mm frame. The cells size is about 30 μm as is shown in Figure 56. The picture was taken by inverse optical microscope "Optika" (faze contrast principle).

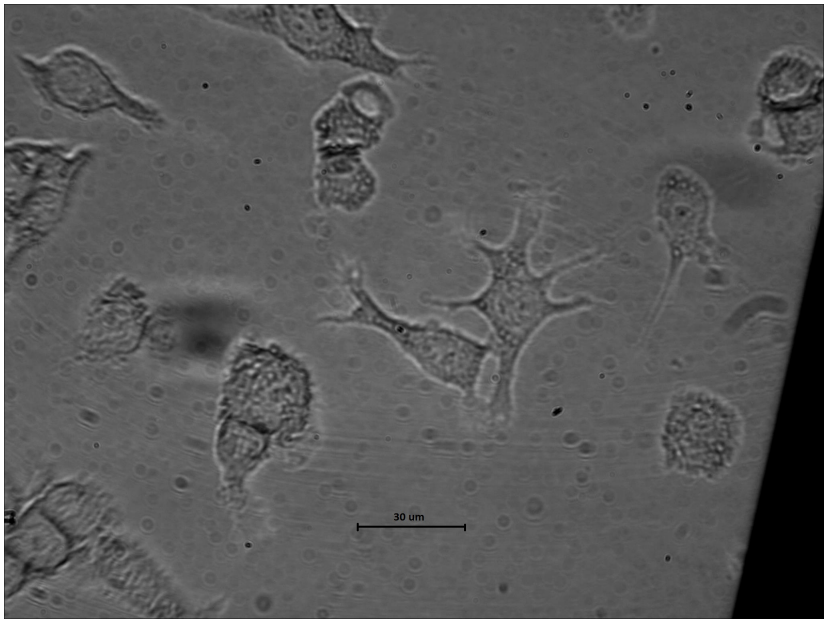

Fig. 56: *CT 26 fibroblasts, derived from colon carcinoma Mus musculus displayed using inverse optical microscope.*

Preparation Procedure

Cells were cultured in Dulbecco's modified eagle's medium (Sigma Aldrich) containing 10% Fetal bovine serum (Gibco) and 1% gentamicin (Sandoz). A droplet (10-20 μl) of the cell suspension in the medium was placed on a Si_3N_4 membrane. Suspension concentration was 1×10^6 cells/ml. The membrane with cells were incubated for 24 h at 37°C in 5% CO_2 atmosphere. For preparation of the samples medium was removed and careful rinsed with PBS (Sigma Aldrich) for 5 min. Then we dehydrated the cells by series of ethanol-distilled water washes.

50% EtOH - 1× - 5 min.
70% EtOH - 1× - 5 min.
80% EtOH - 1× - 10 min.
95% EtOH - 1× - 10 min.
100% EtOH - 2× - 10 min.

6.2 Sample Imaging

Our sample was imaged by SXR source based onto a double-stream gas-puff target. The schema is shown in Figure 57. Imaging was done in collaboration with Institute of Optoelectronics, MUT.

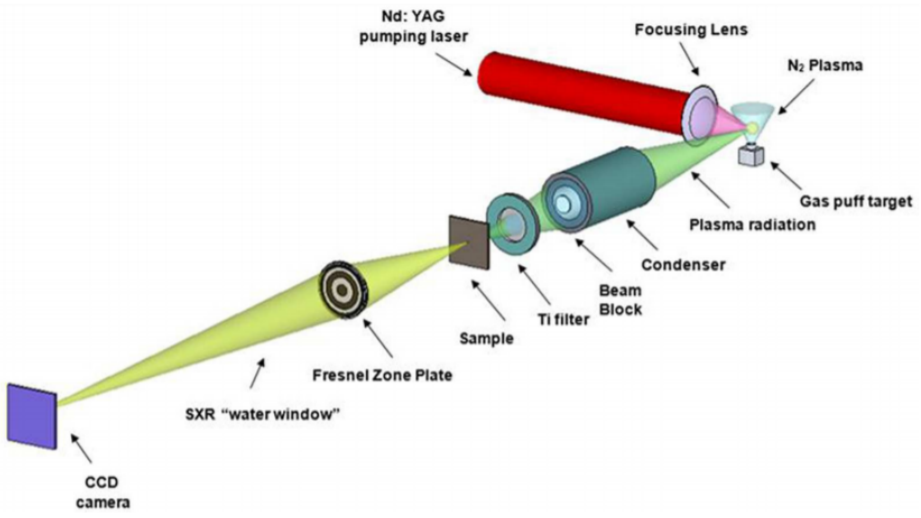

Fig. 57: *Scheme of the water window SXR microscope based a double-stream Nitrogen/Helium gas-puff target source, Fresnel zone plate objective and ellipsoidal condenser. [65]*

We can see in Figure 58 direct comparison between images acquired by a visible light microscope (a, c, e, g) and SXR images of the cells (b, d, f, h). The SXR images were acquired with 200 SXR pulses, 22 s exposure time, source repetition rate of 10 Hz, detector temperature –20°C, while the visible light microscopy images were obtained with 40× objective and NA = 0.7. [66] It is possible to observe cells with internal structure using visible light microscope (phase contrast mode) and due to the modulation in the transmittance of the SXR light through the sample in the SXR images.

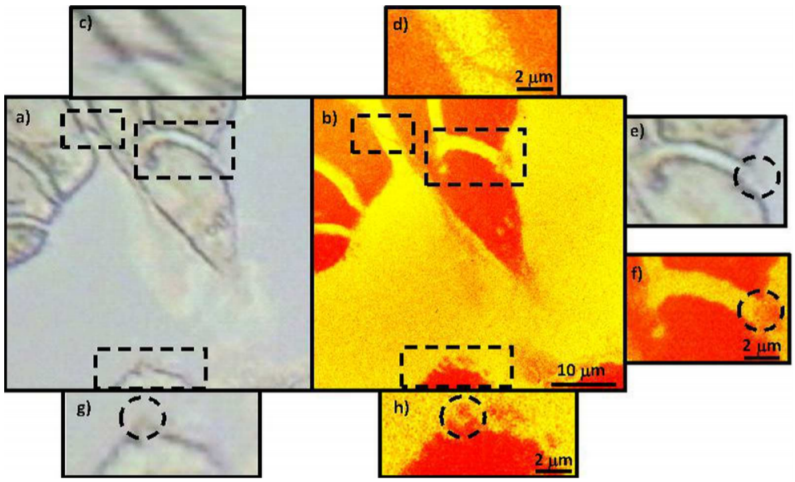

Fig. 58: *Comparison between visible light microscopy images and SXR images of dehydrated CT 26 fibroblasts. [66]*

7 Conclusion

In this work, I have optimized our SXR source, which will be the basis for the SXR microscope in the future to display biological samples. Based on the knowledge of all parameters of the whole system I have defined an optimization function $F(E_{out})$ (chapter 1.5). This function is dependent on nine different parameters and it was necessary to find out correlation and how much they affect the system. My aim was to get maximum output energy E_{out} from the SXR source.

Chapter 3 summarizes the measurement and results of each parameter. These measurements have gradually shown that a number of parameters can be set for our system. Only three parameters of the whole system (mass density ρ, Δz, and Δt) affect significantly the system. This has simplified the optimization function to $F(E_{out}) = F(\, rho, \Delta z, \Delta t)$. The system parameters correlation with recommended settings is given in chapter 4.3.

Special attention was paid to the parameters ρ and Δz. These are parameters influencing the gas-puff target and thus directly the formation of plasma. I performed a series of shadowgraphy measurements at our collaborative laboratory in Warsaw, from which I was able to define target density and the effect of jet ablation on the gas-puff target. The most important results from these measurements are summarized in 4.1 and also published in [57]. The first task was to study the gas-puff target for Nitrogen, Argon, and Krypton (gasses that can be used in our laboratory) when flowing from a new nozzle. Subsequently, I studied the change in the gas-puff target when the nozzle was damaged by use. As has been shown, the particle density in the gas-puff target may be several times lower for a nozzle ablated by use and, moreover, does not show an upward trend in particle density with increasing gas inlet pressure as the new nozzle (Fig. 33). I have shown that, over time, there is a change in the gaseous target and therefore a decrease in the maximum radiated energy of our source. Nozzle damage occurs due to the small distance of the focal plane from the nozzle and subsequent ablation to form a plasma. So I studied the dependence of radiation on the distance of Δz. As can be seen from the graph in Fig. 23, for the increasing Δz, the radiated intensity decreases, which is in contradiction with the maximum output energy requirement. One way of solving the problem with nozzle ablation would be to use a double stream nozzle, as shown in 4.1.1. However, replacing the existing nozzle with a double stream nozzle is not yet planned, as this would mean replacing part of

the system and controls.

In addition to measurements, I also intensively devoted to simulations using 2D radio-magneto-hydro-dynamic code Zstar. My goal was to create a gas-puff target model whose results could then be used to simulate plasma radiation in the same program. So far, no one has dealt with anything like this in Zstar and it was necessary to build not only the model itself but also to verify its functionality. As shown in the graph 44, both the model and the experiment show a match. As a result, I used this model to simulate flow for different gasses, gas input pressures that we are not currently able to achieve in our system or to simulate flow into higher background pressure. Here I followed the publication [63], where an experiment was performed with different density of Helium in the background and various values of nitrogen input pressure. It has been shown that by increasing the background pressure it is possible to obtain a narrower profile of the gas-puff target and to move the focal plane further away from the nozzle while maintaining the density of the target. The result is illustrated in Fig. 47 and 48. The results in chapter 4.2.2 are currently the subject of the forthcoming publication.

Our SXR source is supposed to be the basis of the SXR microscope in the future, therefore the study and preparation of biological samples were an integral part of my work. We chose a sample of CT 26 fibroblasts, derived from colon carcinoma Mus musculus (strain BALB/c). By gradual dehydration, we created several specimens at FBME, depicted at a collaborative workplace at MUT in Warsaw. The imaging results are summarized in chapter 6.2 and in the publications [21, 66].

References

[1] S. Bell, *Introduction to Microscopy*, Taylor and Francis Inc., October 2009. ISBN: 142008450X

[2] D. T. Attwood, *Soft X-Rays and Extreme Ultraviolet Radiation: Principles and Applications*, United States: Cambridge University Press, 2007. 470 s. ISBN 0-521-65214-6.

[3] C. Hagen, P. Guttmann, B. Klupp, S. Werner, S. Rehbein, T. C. Mettenleiter et al., *Correlative VIS-fluorescence and soft X-ray cryo-microscopy/tomography of adherent cells*, Journal of Structural Biology, 177(2), p. 193–201, 2012. DOI: 10.1016/j.jsb.2011.12.012

[4] E. Duke, K. Dent, M. Razi, L. M. Collinson, *Biological applications of cryo-soft X-ray tomography*, Journal of Microscopy, 255(2), p. 65–70, 2014. DOI: 10.1111/jmi.12139

[5] S. Hädrich, A. Klenke, J. Rothhardt, et al., *High photon flux table-top coherent extreme-ultraviolet source*, Nature Photonics, 8(10), p. 779–783, 2014. DOI: 10.1038/nphoton.2014.214

[6] P. Vrba, S. V. Zakharov, A. Jancarek, M. Vrbova, M. Nevrkla, *Pinching capillary discharge as a water window radiation source*, Journal of Electron Spectroscopy and Related Phenomena, Volume 184, Issues 3–6, April 2011, Pages 335-337, ISSN 0368-2048, 10.1016/j.elspec.2010.12.013.

[7] H. Leggal, G. Blobel, H. Stiel et al., *Compact x-ray microscope for the water window based on a high brightness laser plasma source*, Optics Express, vol. 20, issue 16, s. 18362, 2012. DOI: 10.1364/OE.20.018362

[8] J. Kirz, Ch. Jacobsen, M.R. Howells, *Soft X-ray microscopes and their biological applications*, Quarterly Reviews of Biophysics. 28, 33130, 1995. DOI: 10.1017/S0033583500003139

[9] K. Takaba, M. Hoshino, S. Aoki, *Simple method of confirming wet environment for soft X-ray microscopy to observe hydrated biological specimens*, Japanese Journal of Applied Physics, 51(9), 2012. DOI: 10.1143/JJAP.51.092401

[10] P. Skoglund, U. Lundström, U. Vogt, H. M. Hertz, *High-brightness water-window electron-impact liquid-jet microfocus source*, Applied Physics Letters, 96(8), 2010. DOI: 10.1063/1.3310281

[11] M. Müller, T. Mey, J. Niemeyer, K. Mann, *Table-top soft x-ray microscope using laser-induced plasma from a pulsed gas jet*, Optics Express, 22(19), 23489, 2014. DOI: 10.1364/oe.22.023489

[12] *X-Ray Properties of the Elements* [on-line]. 1997 [cit. 2012-06-14]. *henke.lbl.gov/optical_constants/pert_form.html*

[13] A. Köhler, *Gedanken zu einem neuen Beleuchtungsverfahren für mikrophotographische Zwecke*, Zeitschrift für wissenschaftliche Mikroskopie, 1893.

[14] J. B. Pawley (ed.), *Handbook of biological confocal microscopy*, 3^{rd} edition, Springer-Verlag New York Inc., 2006.

[15] M. Knoll, E. Ruska, *Das Elektronenmikroskop*, Z. Phys. A: Hadrons Nucl. 78, p. 318-339, 1932. DOI: 10.1007/BF01342199

[16] R. Erni, M. D. Rossell, C. Kisielowski and U. Dahmen, *Atomic-Resolution Imaging with a Sub-50-pm Electron Probe*, Phys. Rev. Lett. 102, 096101, 2009. DOI: 10.1103/PhysRevLett.102.096101

[17] W. C. Röntgen, *Über eine neue Art von Strahlen*, Sitzungsberichte der physikalisch-medizinischen Gesellschaft, p. 137-141, 1895.

[18] A. Bayer, F. Barkusky, S. Döring, P. Großmann, K. Mann, *Applications of Compact Laser-Driven EUV/XUV Plasma Sources*; X-Ray Optics and Instrumentation Volume 2010, Article ID 687496, 9 pages, 2010. DOI: 10.1155/2010/687496

[19] P. Wachulak, A. Bartnik, M. Skorupka et al., *Water-window microscopy using a compact, laser-plasma SXR source based on a double-stream gas-puff target*, Applied Physic B, Lasers and Optics, p. 239–247, 2013. DOI: 10.1007/s00340-012-5324-y

[20] H. M. Hertz, M. Berglund, G. A. Johansson, M. Peuker, T. Wilhein and H. Brismar, *Compact water-window x-ray microscopy with a droplet laser-plasma source*, AIP Conf. Proc. 507, 721, 2000. DOI: 10.1063/1.1291239

[21] A. Torrisi, P. Wachulak, M. Nawaz, A. Bartnik, D. Adjei, S. Vondrova et al., *Applications of a Compact "Water Window" Source for Investigations of Nanostructures Using SXR Microscope*, Acta Physica Polonica A, 129, p. 169-171,2016. DOI: 10.12693/APhysPolA.129.169

[22] J. Kirz, Ch. Jacobsen, M. Howells, *Soft-X-Ray Microscopes and Their Biological Applications*, Quarterly reviews of biophysics, 28. p. 33-130, 1995. DOI: 10.1017/S0033583500003139

[23] P. Wachulak, A. Bartnik, H. Fiedorowicz: Nanoimaging using a compact laser plasma soft x-ray source based on a gas puff target, Proceedings Volume 11112, X-Ray Nanoimaging: Instruments and Methods IV; 111120V, 2019. DOI: 10.1117/12.2529468

[24] G. Schmahl, D. Rudolph, B. Niemann, P. Guttmann, J. Thieme et al., *X-ray microscopy studies*, Optik 93, p. 95–102, 1993.

[25] Ch. Spielmann, M. Schnürer, N. H. Burnett et al., *Generation of coherent XUV radiation in water window*, 10.1109/CLEO.1998.675894, 1998. DOI: 10.1109/CLEO.1998.675894

[26] M. Berglund, L. Rymell, M. Peuker, T. Wilhein, H. M. Hertz, *Compact water-window transmission X-ray microscopy*, Journal of Microscopy, Vol. 197, p. 268-273, 2000. DOI: 10.1046/j.1365-2818.2000.00675.x

[27] S. Vondrova, *Optimalization of Laser Plasma in a Gas Target as a Source of XUV Radiation for Applications in Biomedicine*, Prague, 2011, Diploma Thesis, Czech Technical University in Prague, Faculty of Electrical Engineering, Supervisor: M. Vrbova.

[28] P. W. Wachulak, A. Bartnik, H. Fiedorowicz, D. Panek, P. Bruza, *Imaging of nanostructures with sub-100 nm spatial resolution using a desktop EUV microscope*, Applied Phys. B-Lasers and Optics, Vol. 109, Is. 1, p. 105-111, 2012. DOI: 10.1007/s00340-012-5125-3

[29] H. Legall, G. Blobel, H. Stiel, W. Sandner, C. Seim et al., *Compact x-ray microscope for the water window based on a high brightness laser plasma source*, Optics Express, Vol. 20, No. 16, 2012.

[30] M. Müller, T. Mey, J. Niemeyer, K. Mann, *Table-top soft x-ray microscope using laser-induced plasma from a pulsed gas jet*, Optics Express, 22(19), 23489, 2014. DOI: 10.1364/oe.22.023489

[31] M. Kishimoto, M. Kado, M. Ishino, S. Tamotsu, K. Yasuda, K. Shinohara, *Development of single shot soft x-ray contact microscopy system for nano-scale dynamics measurement of living biological specimen*, AIP Conf. Proc. 1465, p. 43-47, Japan, DOI: /10.1063/1.4737537

[32] A. G. Michette, *Optical systems for soft X rays*, New York: Plenum Press, 1986. DOI: 10.1007/978-1-4613-2223-8

[33] R. Serway; C. Moses and C. Moyer, *Modern Physics*, 2'nd edition, Sounders College Publishing, 1997.

[34] M. Bertilson, *Laboratory Soft X-Ray Microscopy and Tomography*, Ph.D. Thesis, Royal Institute of Technology, Stockholm, Sweden, 2011.

[35] R. D. L. Kronig, *On the theory of dispersion of x-rays*, J. Opt. Soc. Am. 12, p. 547-556, 1926.

[36] V. Kanicky, *Emisní spektrální analýza* [online]. Brno, Masarykova univerzita v Brně, 2009 [cit. 2011-03-23]. *cheminfo.chemi.muni.cz/chem_sekce/predmety/C7300/AES/Emisni%20spektralni%20analyza.pdf*

[37] J. P. Boeuf and L. C. Pitchford, *Pseudospark discharges via computer simulation*, IEEE T. Plasma Sci. 19, p. 286-296, 1991.

[38] M. Benk, K. Bergmann, D. Schäfer and T. Wilhein, *Compact soft x-ray microscope using a gas-discharge light source*, Opt. Lett. 33, p. 2359-2361, 2008.

[39] M. Benk, D. Schafer, T. Wilhein and K. Bergmann, *High power soft x-ray source based on a discharge plasma*, J. Phys.: Conf. Ser. 186, 012024, 2009.

[40] *EQ-10SXR Soft X-Ray Source*, Energetiq [on-line]. 2012 [cit. 2013-10-12]. *www.energetiq.com/DataSheets/EQ10SXR_DataSheet.pdf*

[41] E. S. Wyndham, M. Favre, M. P. Valdivia, J. C. Valenzuela, *Considerations of a high repitition Capillary Discharge operated in nitrogen as a water-window X-ray*

microscope source, Pulsed Power Conference, PPC '09. IEEE , pp.688-692, 2009, doi: 10.1109/PPC.2009.5386387

[42] *Table-Top EUV / XUV Source: Manual*, Vers. 1.0, Laser-Laboratorium Göttingen e.V., 2010.

[43] *AXUV20HS1 Datasheet* IRD, California, p. 41, 2009. *www.alldatasheet.com/datasheet−pdf/pdf/*531872/*OPTODIODE/AXUV*20*HS*1.*html*

[44] P. A. C. Takman, H. Stollberg, G. A. Johansson, A. Holmberg, M. Lindblom, H. M. Hertz *High-resolution compact X-ray microscopy*, The Royal Microscopical Society, 2007. DOI: 10.1111/j.1365-2818.2007.01765.x

[45] H. M. Hertz, O. von Hofsten, M. Bertilson, U. Vogt, A. Holmberg, J. Reinspach, D. Martz et al., *Laboratory Cryo Soft X-Ray Microscopy*, Journal of Structural Biology 177 (2): p. 267–72, 2012. DOI: 10.1016/j.jsb.2011.11.015

[46] D.Y. Parkinson, C. Knoechel, C. Yang, C. A. Larabell and M. A. Le Gros, *Automatic alignment and reconstruction of images for soft X-ray tomography*, Journal of Structural Biology 177, p. 259–266, 2012. DOI: 10.1016/j.jsb.2011.11.027

[47] D. Shapiro, P. Thibault, D. Sayre, *Biological imaging by soft x-ray diffraction microscopy*, Proceedings of the National Academy of Sciences of the United States of America 102, p. 15343–15346, 2005. DOI:10.1073/pnas.0503305102

[48] F. Bonfigli, F. Flora, A. Lai, M. Vincenti, *Soft X-ray contact microscopy of dry biological samples and in vivo plant cells on high spatial resolution lithium fluoride fluorescent imaging detectors* 680.

[49] K. Takemoto, S. Ichise, T. Ohigashi, H. Namba, H. Kihara, *X-ray imaging of mucilaginous sheath of phytoplankton in lake biwa by soft X-ray microscope*, AIP Conference Proceedings 1365, p. 373–376, 2010. DOI: 10.1063/1.3625381

[50] I. H. Munro et al., *Confocal imaging using synchrotron radiation*, Journal of Electron Spectroscopy and Related Phenomena, 80, p. 343–347, 1996. DOI: 10.1016/0368-2048(96)02988-X

[51] W. Meyer-Ilse et al., *High resolution protein localization using soft X-ray microscopy*, Journal of Microscopy. 201, p. 395–403, 2001.

[52] S. Vondrova, T. Parkman, M. Vrbova, *Comparison of LPP and DPP in Nitrogen Source*, ECLIM 2014 Conference Proceedings, Paris, France, 2014.

[53] S. Kranzusch and K. Mann, *Spectral characterization of EUV radiation emitted from a laser-irradiated gas puff target*, Optics Communications, vol. 200, no. 1–6, pp. 223–230, 2001. DOI: 10.1016/S0030-4018(01)01639-X

[54] S. Vondrova, M. Vrbova, D. Panek, P. Bruza, P. Vrba et al., *Diagnostics and Modeling of Gas Puff Target Laser Plasma Radiation Source*. In 2012 International Workshop on EUV and Soft X-Ray Sources. Austin: EUV Litho Inc, p. 11+, 2012.

[55] R. Rakowskia A. Bartnik, H. Fiedorowicz, *Pulsed X-ray radiography of a gas jet target for laser–matter interaction experiments with the use of a CCD detector*, Nuclear Instruments and Methods in Physics Research A 551, p. 139 - 144, 2005. DOI: 10.1016/j.nima.2005.07.047

[56] Laser-Matter Interaction Group, Military University of Technology, Warsaw, [online], [cit. 2019-09-23] *www.ztl.wat.edu.pl/zoplzm/index_eng.html*

[57] S. Salacova, P. Wachulak, M. Taticek, M. Vrbova, *Gas-Puff Target for Laser-Producing Plasma SXR Source*, Acta Polytechnica, Vol. 59, No. 6, 2019. DOI: 10.14311/AP.2019.59.0587

[58] P. W. Wachulak, A. Torrisi, A., Bartnik, D. Adjei, J. Kostecki, L. Wegrzynski, H. Fiedorowicz, *Desktop water window microscope using a double-stream gas puff target source*, Applied Physics B: Lasers and Optics, 118(4), p. 573–578, 2015. DOI: doi.org/10.1007/s00340-015-6044-x

[59] V. Bakshi, *EUV Sources for Lithography*, SPIE Press, 1094 pages2006. ISBN: 9780819458452

[60] S. V. Zakharov, A. F. Nikiforov and V. G. Novikov, *ZETA code: Physical Models and Numerical Algorithms*, KIAM report, Moscow, 1994.

[61] *ANSYS* [online], [cit. 2020-01-26]. *www.ansys.com*

[62] A. K. Rebrov, *Free jets in vacuum technologies*, Journal of Vacuum Science & Technology A: Vacuum, Surfaces, and Films, p. 1679-1687, 2001. DOI: 10.1116/1.1382649

[63] T. Mey, M. Rein, P. Großmann, K. Mann, *Brilliance improvement of laser-produced soft x-ray plasma by a barrel shock*, New Journal of Physics, 14, 2012. DOI:10.1088/1367-2630/14/7/073045

[64] H. Ashkenas, F. S. Sherman, *The structure and utilization of supersonic free jets in low density wind tunnels*, Fourth Symp. on Rarefied Gas Dynamics, vol II, p. 84–105, 1966.

[65] P. W. Wachulak, A. Torrisi, A. Bartnik, et al., *Desktop water window microscope using a double-stream gas puff target source*, Applied Physics B: Lasers and Optics, 118(4), p. 573–578, 2015. DOI: 10.1007/s00340-015-6044-x

[66] P. Wachulak, A. Torrisi, M. Ayele, A. Bartnik, J. Czwartos,L. Wegrzynski, T. Fok, T. Parkman, S. Vondrova et al. *Soft X-Ray Imaging With Incoherent Sources*, Proceedings Of Spie, Volume 10243, 2017.

8 My Publications

1 S. Vondrova, M. Vrbova, *Optimalization of laser plasma in a gas target as a source of XUV radiation for applications in biomedcine*, Instruments and methods for biology and medicine 2011. Praha: CTU Publishing House, s. 127, 2011. ISBN: 978-80-01-04915-0

2 S. Vondrova, *Optimalization of Laser Plasma in a Gas Target as a Source of XUV Radiation for Applications in Biomedicine*, Prague, 2011, Diploma Thesis, Czech Technical University in Prague, Faculty of Electrical Engineering, Supervisor: M. Vrbova.

3 S. Vondrova, M. Vrbova, *Pulsed X-RAY radiography of a various gas puff target*, Instuments and Methods for Biology and Medicine 2012. Prague: Czech Technical University, 2012. ISBN: 978-80-01-05119-1

4 S. Vondrova, M. Vrbova, D. Panek, P. Bruza, P. Vrba et al., *Diagnostics and Modeling of Gas Puff Target Laser Plasma Radiation Source.* In 2012 International Workshop on EUV and Soft X-Ray Sources. Austin: EUV Litho Inc, p. 11+, 2012.

5 S. Vondrova, T. Parkman, M. Vrbova, *Comparison of LPP and DPP in Nitrogen Source*, ECLIM 2014 Conference Proceedings, Paris, France, 2014.

6 P. W. Wachulak, A. Torrisi, M. F. Nawaz, A. Bartnik, D. Adjei, S. Vondrova, et al., *A Compact "Water Window" Microscope with 60 nm Spatial Resolution for Applications in Biology and Nanotechnology*, Microscopy And Microanalysi, Vol. 21, Issue 5, Page 1214-1223, 2015. DOI: 10.1017/S1431927615014750

7 P. W. Wachulak, A. Torrisi, M. F. Nawaz, A. Bartnik, D. Adjei, J. Jostecki, L. Wegrzynski, S. Vondrova, ae al., *A Compact "Water-Window" Microscope With 60 Nm Spatial Resolution Based On A Double Stream Gas-Puff Target And Fresnel Zone Plate Optics*, Euv And X-Ray Optics: Synergy Between Laboratory And Space IV, Volume 9510, 2015. DOI: 10.1117/12.2181431

8 A. Torrisi, P. W. Wachulak, M. F. Nawaz, A. Bartnik, D. Adjei, S. Vondrova, et al., *Applications of a Compact "Water Window" Source for Investigations of*

Nanostructures Using SXR Microscope, Acta Physica Polonica, A., Vol. 129 Issue 2, p169-171, 2016. DOI: 10.12693/APhysPolA.129.169

9 A. Torrisi, P. W. Wachulak, Ł. Węgrzyński, T. Fok, A. Bartnik, T. Parkman, S. Vondrova, et al., *A stand-alone compact EUV microscope based on gas-puff target source*, Journal of Microscopy, 265, Vol. 2, 02/2017. DOI: 10.1111/jmi.12494

10 P. W. Wachulak, A. Torrisi, M. Ayele, A. Bartnik, J. Czwartos, L. Wegrzynski, T. Fok, T. Parkman, S. Vondrova, et al., *Soft X-Ray Imaging With Incoherent Sources*, Proceedings Of Spie, Volume 10243, 2017. DOI: 10.1117/12.2265093

11 S. Salacova, P. Wachulak, M. Taticek, M. Vrbova, *Gas-Puff Target for Laser-Producing Plasma SXR Source*, Acta Polytechnica, Vol. 59, No. 6, 2019. DOI: 10.14311/AP.2019.59.0587

Editorial activity:

A S. Vondrova, M. Taticek, *Instruments and Methods for Biology and Medicine 2014*, conference proceedings, Prague: Czech Technical University, 2015. ISBN 978-80-01-05636-3.

B S. Vondrova, M. Taticek, *Instruments and Methods for Biology and Medicine 2015*, conference proceedings, Prague: Czech Technical University, 2015. ISBN 978-80-01-05851-0.

C S. Vondrova, *Instruments and Methods for Biology and Medicine 2016*, conference proceedings, Prague: Czech Technical University, 2016, [on-line] $imbm.fbmi.cvut.cz/soubory/Proceeding\%20IMBM\%202016-web.pdf$

9 Acknowledgements

This work would not have been possible without the contributions and support of many. I wish to express my gratitude to all of them.

I would like to thank my supervisor prof. Vrbová, who gave me the opportunity to find out new fields of study, broaden my horizons and met new interesting and inspiring people. Thanks to her, I discovered new possibilities and my limits.

Great thanks belong to my colleagues, who joined me in their research, for their patience and help. I appreciate our many discussions on science, choice of career and life in general. They helped me set my priorities and find new challenges. The support from Milan Tatíček helped me to avoid lecturing mistakes and align the new and challenging role as a teacher. Also, the cooperation with Tomáš Parkman was one of the bright points of my studies. We cooperated on many conferences organization, presentation for new students and the general public.

I can not forget to thanks all other colleagues Dalibor, Martin, Petr, Honza, Jana, and Hanka, who each influenced me in some way and helped me with my professional and personal development.

The biggest thanks belong to my beloved family for their support, encouragement, love, and patience. Sometimes, I was lost and wanted to quit, but I was always with my husband, who encouraged me and allowed me to do scientific work.